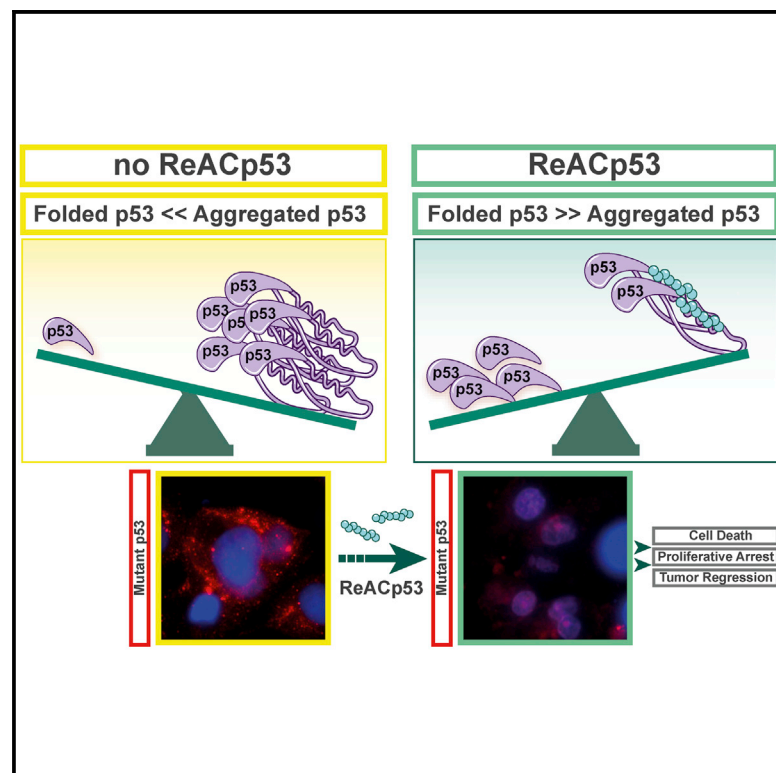


A Designed Inhibitor of p53 Aggregation Rescues p53 Tumor Suppression in Ovarian Carcinomas

Graphical Abstract



Authors

Alice Soragni, Deanna M. Janzen, Lisa M. Johnson, ..., Matteo Pellegrini, Sanaz Memarzadeh, David S. Eisenberg

Correspondence

david@mbi.ucla.edu (D.S.E.), smemarzadeh@mednet.ucla.edu (S.M.)

In Brief

Using p53-mutant, high-grade, serous ovarian carcinoma as model systems, Soragni et al. show that a cell-penetrating peptide designed to inhibit p53 amyloid formation rescues p53 functions and reduces in vivo xenograft growth and metastasis.

Highlights

- We designed the peptide ReACp53 to halt aggregation of p53 in cells
- ReACp53 rescues p53 transcription of target genes and restores apoptosis
- In vivo ReACp53 halts progression and shrinks tumors bearing aggregation-prone p53
- p53 aggregation in cancer is a target for therapy with ReACp53 as a lead compound

Accession Numbers

4RP6
4RP7
GSE74550



A Designed Inhibitor of p53 Aggregation Rescues p53 Tumor Suppression in Ovarian Carcinomas

Alice Soragni,¹ Deanna M. Janzen,² Lisa M. Johnson,¹ Anne G. Lindgren,² Anh Thai-Quynh Nguyen,^{1,8} Ekaterina Tiourin,² Angela B. Soriaga,¹ Jing Lu,³ Lin Jiang,^{1,9} Kym F. Faull,⁴ Matteo Pellegrini,³ Sanaz Memarzadeh,^{2,5,6,7,*} and David S. Eisenberg^{1,7,*}

¹Departments of Biological Chemistry and Chemistry and Biochemistry, UCLA-DOE Institute, HHMI, 611 South Charles E. Young Drive, Los Angeles, CA 90095-1570, USA

²Department of Obstetrics and Gynecology, David Geffen School of Medicine, University of California Los Angeles, Los Angeles, CA 90095, USA

³Molecular, Cell and Developmental Biology, University of California Los Angeles, Los Angeles, CA 90095, USA

⁴Pasarow Mass Spectrometry Laboratory, Semel Institute, 405 Hilgard Avenue, Los Angeles, CA 90095, USA

⁵Eli and Edythe Broad Center of Regenerative Medicine and Stem Cell Research, University of California Los Angeles, Los Angeles, CA 90095, USA

⁶The VA Greater Los Angeles Health Care System, Los Angeles, CA 90073, USA

⁷Co-senior author

⁸Present address: Laboratory of Stem Cell Research and Application, University of Science, Vietnam National University, Ho Chi Minh City, Vietnam

⁹Present address: Department of Neurology, Mary S. Easton Center for Alzheimer's Disease Research, David Geffen School of Medicine, University of California at Los Angeles, Los Angeles, CA 90095, USA

*Correspondence: david@mbi.ucla.edu (D.S.E.), smemarzadeh@mednet.ucla.edu (S.M.)

<http://dx.doi.org/10.1016/j.ccell.2015.12.002>

SUMMARY

Half of all human cancers lose p53 function by missense mutations, with an unknown fraction of these containing p53 in a self-aggregated amyloid-like state. Here we show that a cell-penetrating peptide, ReACp53, designed to inhibit p53 amyloid formation, rescues p53 function in cancer cell lines and in organoids derived from high-grade serous ovarian carcinomas (HGSOC), an aggressive cancer characterized by ubiquitous p53 mutations. Rescued p53 behaves similarly to its wild-type counterpart in regulating target genes, reducing cell proliferation and increasing cell death. Intraperitoneal administration decreases tumor proliferation and shrinks xenografts in vivo. Our data show the effectiveness of targeting a specific aggregation defect of p53 and its potential applicability to HGSOCs.

INTRODUCTION

p53 is a tumor suppressor of paramount importance and the most frequently mutated protein in human cancers (Lane and Crawford, 1979; Levine and Oren, 2009; Linzer and Levine, 1979). It arrests proliferation and promotes either DNA repair or apoptosis in cells with DNA damage or under stresses such as hypoxia or starvation (Vazquez et al., 2008; Vousden and Ryan, 2009). In over half of all tumors, p53 is inactivated by a single point mutation, most frequently in the DNA binding domain.

These mutations inactivate the protein, either by altering a residue that directly contacts DNA (contact mutants) or by mutating a residue that destabilizes and partially unfolds p53 (structural mutants), although the separation between classes is not absolute (Joerger and Fersht, 2008).

Depending on cancer type, the percentage of cases bearing p53 mutations varies. One of the subtypes presenting with the highest prevalence are high-grade serous ovarian carcinomas (HGSOC), where mutations are reported in >96% of cases (Cancer Genome Atlas Research Network, 2011; Ahmed et al.,

Significance

Among all cancers, HGSOC has the highest rate of p53 mutations and no curative therapies, so it is an ideal test system for p53-reactivating molecules such as ReACp53. Because aggregation of p53 has been observed in a variety of tumors, ReACp53 can also be applied to other cancers. By inhibiting p53 aggregation, ReACp53 alters the dynamic equilibrium between folded, partially unfolded, and aggregated p53, re-instating a pool of functional wild-type-like protein capable of driving tumor regression. ReACp53 rescues the function of two of the most commonly mutated residues, R175 and R248. While many mutants may aggregate and respond to ReACp53, these two alone are present in tumors of ~80,000 U.S. patients/year, who could potentially benefit from a p53-aggregation inhibition therapy.

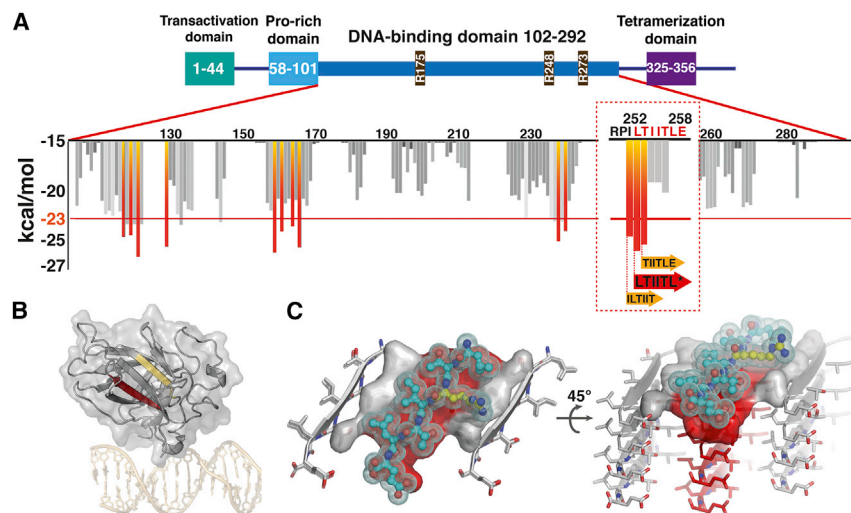


Figure 1. p53 Aggregation Propensity and ReAcP53 Docking on the p53_{252–258} Amyloid Zipper Structure

(A) ZipperDB (<http://services.mbi.ucla.edu/zipperdb/>) predicts multiple segments in the p53 DNA-binding domain as aggregation prone. The highest propensity ones are located in the 252–258 region. Colored bars indicate aggregation-prone segments with Rosetta energies below –23 kcal/mol.

(B) The 252–258 segment (red) is mapped on the p53 DNA-binding domain structure. The segment in yellow (residues 213–217) is the epitope recognized by the PAb240 antibody, which binds to partially unfolded p53. Both segments are buried in the p53 structure when the protein is fully folded. DNA is in gold.

(C) The ReAcP53 peptide (ball-and-stick; cyan, blue, and red represent carbon, nitrogen, and oxygen atoms, respectively) is modeled on the p53_{252–258} amyloid steric zipper structure determined in this study (PDB: 4RP6). The arginine in

position 3 (in yellow) creates a steric clash with the adjacent β sheet and additionally impedes incoming molecules from adhering on top while binding to the steric zipper below. Three adjacent β sheets (in gray and red) of the p53 amyloid spine structure are shown viewed down (left) or nearly perpendicular to the fibril axis (right).

See also Tables S1 and S2 and Figure S1.

2010). Ovarian cancer is the most lethal of all gynecologic cancers and the fifth most common cause of cancer-related death among women in the United States (Siegel et al., 2014). About 80% of all ovarian cancers are of the high-grade serous type, mostly diagnosed at advanced stages with poor long-term prognosis (Seidman et al., 2004). Despite surgical debulking and administration of platinum-based chemotherapy, almost all patients suffer from recurrent and disseminated disease and the majority dies in less than 5 years (Vaughan et al., 2011). Efforts aimed at developing new therapeutic approaches have largely been unsuccessful. An early event in carcinogenesis, p53 inactivation through mutation is associated with poor response to treatment and poor prognosis (Kurman and Shih, 2008; Leitao et al., 2004). Although p53 alterations are so prevalent in ovarian cancer, there is as of yet no targeted therapy approved for restoring p53 function.

Over the past decade, p53 and fragments thereof have been shown to aggregate in vitro (Silva et al., 2014). More recently, several p53 mutants were found as amyloid aggregates in tumor cell lines (Xu et al., 2011) and breast cancer biopsies (Levy et al., 2011). These aggregates inactivate p53 by sequestering the protein, thus blocking its transcriptional activity and pro-apoptotic function (Xu et al., 2011).

Our working hypothesis based on the behavior of other amyloid-forming proteins (Eisenberg and Jucker, 2012), is that each aggregation-promoting mutation initially destabilizes the native protein structure causing exposure of an adhesive sequence (Wang and Fersht, 2012). This segment binds to like segments from other p53 molecules, resulting in protein aggregation and inactivation. The following questions related to p53 aggregation are presently unanswered: (1) Can inhibition of p53 aggregation in these cells rescue normal p53 function? (2) Does such reactivation halt cell proliferation and diminish tumor size in vivo? (3) Does reactivation of p53 avoid on-target toxicities in normal tissues?

Here we address these questions by designing a cell-permeable 17-residue peptide inhibitor of p53 aggregation. Reflecting the intended function of this inhibitor as a rescuer of the activity of p53, we call it ReAcP53.

RESULTS

p53 Amyloid Spine Structure and Its Use to Design a Sequence-Specific Aggregation Inhibitor

Several segments in the DNA binding domain of p53 are prone to form an amyloid adhesive segment, termed a steric zipper, as calculated by the ZipperDB algorithm, which identified residues 252–258 as the most aggregation prone in this region (Figure 1A, Goldschmidt et al., 2010). Segment 251–257 has been reported as necessary and sufficient to drive p53 aggregation in cell lines (Ghosh et al., 2014; Xu et al., 2011). We focused on the two partially overlapping segments 252–LTIITLE-258 and 253–TIITLE-258, and chemically synthesized them. Both formed amyloid-like fibrils and microcrystals that enabled their structure determination at atomic resolution (Sawaya et al., 2007; Figure S1 and Table S1). The segments aggregated as tight, dry steric zippers, with LTIITLE forming a class 2, face-to-back amyloid spine while TIITLE formed a class 1, face-to-face interface. Since both shared similar side-chain contacts, we were able to design an inhibitor that can interact with both and block further aggregation.

Next, we implemented a modified rational approach to design a peptidic inhibitor starting from the LTIITLE structure (Sievers et al., 2011). In order to maximize sequence specificity and avoid off-target effects, we kept the original p53 sequence, but included single or double aggregation-inhibiting residues such as K or R (Ghosh et al., 2014; Härd and Lendel, 2012) in critical positions as judged by the side-chain arrangement in the LTIITLE structure we determined. Various residues were replaced in position 1, 3, and 5 (Table S2), and segments were computationally analyzed with Rosetta to score their structural complementarity

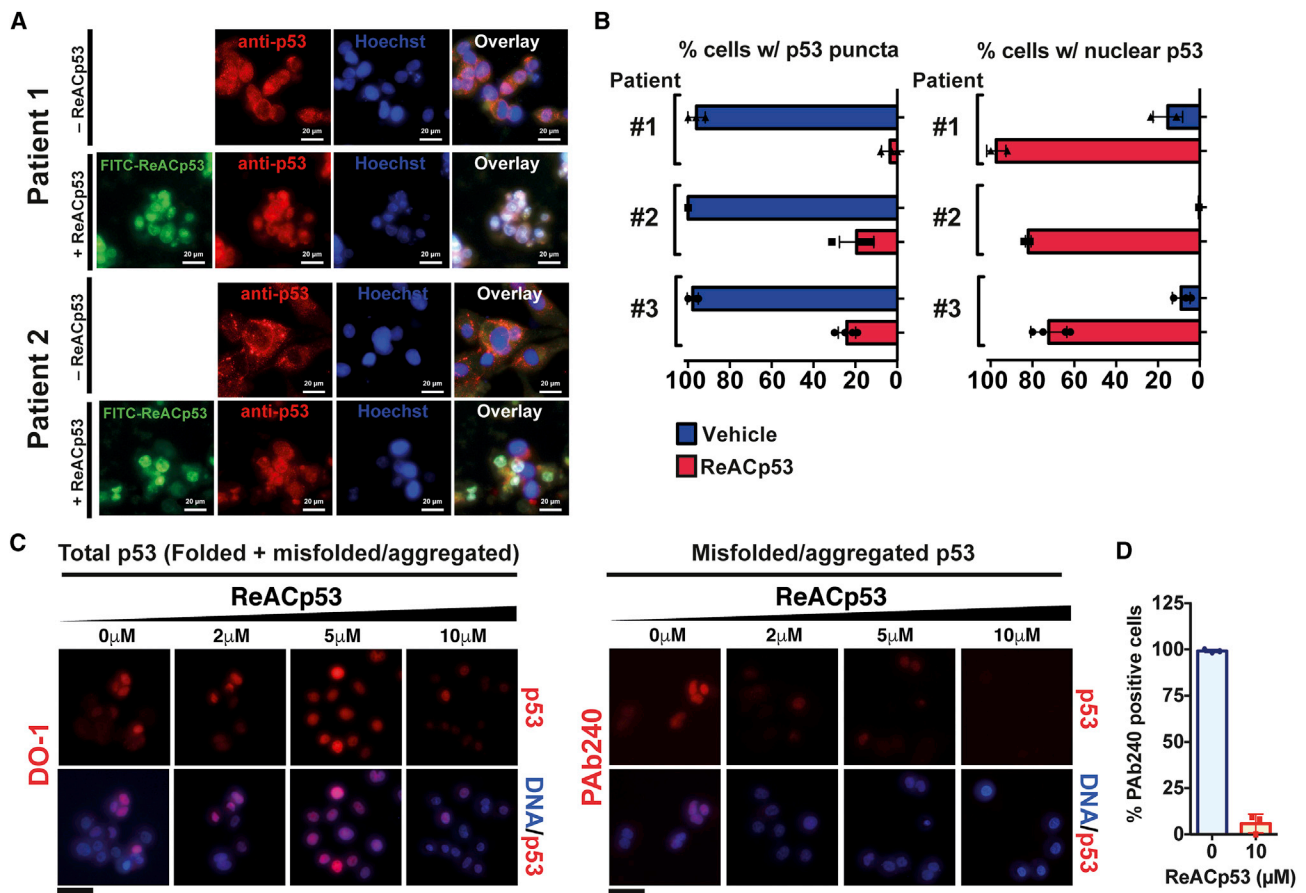


Figure 2. ReACp53 Inhibits p53 Aggregation in Primary Cells from HGSOC Patients, and Relocalizes p53 to the Nucleus in an Active Conformation

(A) Mutant p53 forms aggregates appearing as puncta in the cytosol of primary cells from two HGSOC patients (see Figure S2A for additional examples). ReACp53 reduced the number of cells with puncta and caused p53 to localize to the nucleus. Scale bar, 20 μ m.

(B) Quantification of the number of cells with aggregated p53 and nuclear p53 in three clinical samples. The number of cells with puncta or nuclear p53 counted in 3–5 different fields of view was expressed as % of the total number of cells \pm SD; symbols represent the values for the individual fields of view; bars are average values.

(C) DO-1, an antibody that recognizes p53 regardless of its conformation, binds to p53 in S1 GODL cells over a range of ReACp53 concentrations. PAb240, a conformation-specific antibody that binds only to mutant-like, inactive p53, recognizes and stains p53 in untreated cells, but not in ReACp53-treated cells, indicating that ReACp53 restores p53 to an active conformation. Scale bars, 50 μ m.

(D) Quantification of PAb240 staining; the number of positively stained cells in 3–5 different field of views is expressed as the % of the total number of cells \pm SD. Symbols represent % calculated for the individual field of views, bars are average values.

See also Tables S3 and S4 and Figure S2.

to the original template (Leaver-Fay et al., 2011). Candidate peptides were screened for their ability to inhibit aggregation of the target sequence in vitro and for specificity, and the best candidate with sequence LTRITL was selected for further studies. When mapped onto the atomic structure of the LTIITL segment, the arginine substitution in position 3 clashes with the binding of additional LTIITL molecules (Figure 1C). Experiments confirmed that LTRITL efficiently blocks peptide aggregation in vitro (Figure S1G), with marked effects at substoichiometric concentrations. Although full-length p53 harboring the I254R mutation does not aggregate in cells (Xu et al., 2011), there is no guarantee that an exogenously administered LTRITL peptide may work as an efficient inhibitor so we proceeded to test this hypothesis. We fused the peptide to an N-terminal poly-arginine cell-penetrating tag (R = 9; Fuchs and Raines, 2005), fol-

lowed by a three-residue linker derived from the p53 sequence (RPI) and tested this candidate, ReACp53, in cells.

ReACp53 Penetrates into HGSOC Primary Cancer Cells and Converts Mutant p53 from a Punctate State into Soluble Wild-type-like p53

We isolated primary cells from a cohort of HGSOC patients ($n = 7$, Table S3) bearing various p53 mutations. We confirmed that ReACp53 could enter the cells by chemically coupling it to a fluorescein isothiocyanate (FITC) moiety. Cells treated with 10 μ M FITC-labeled peptide for 16–20 hr in serum-free medium showed intracellular and intranuclear staining, indicative of ReACp53 penetration (Figures 2A, S2A, S2B, and S2E).

When primary cells grown on coverslips were stained for p53, all patient samples harboring the R248Q mutation exhibited

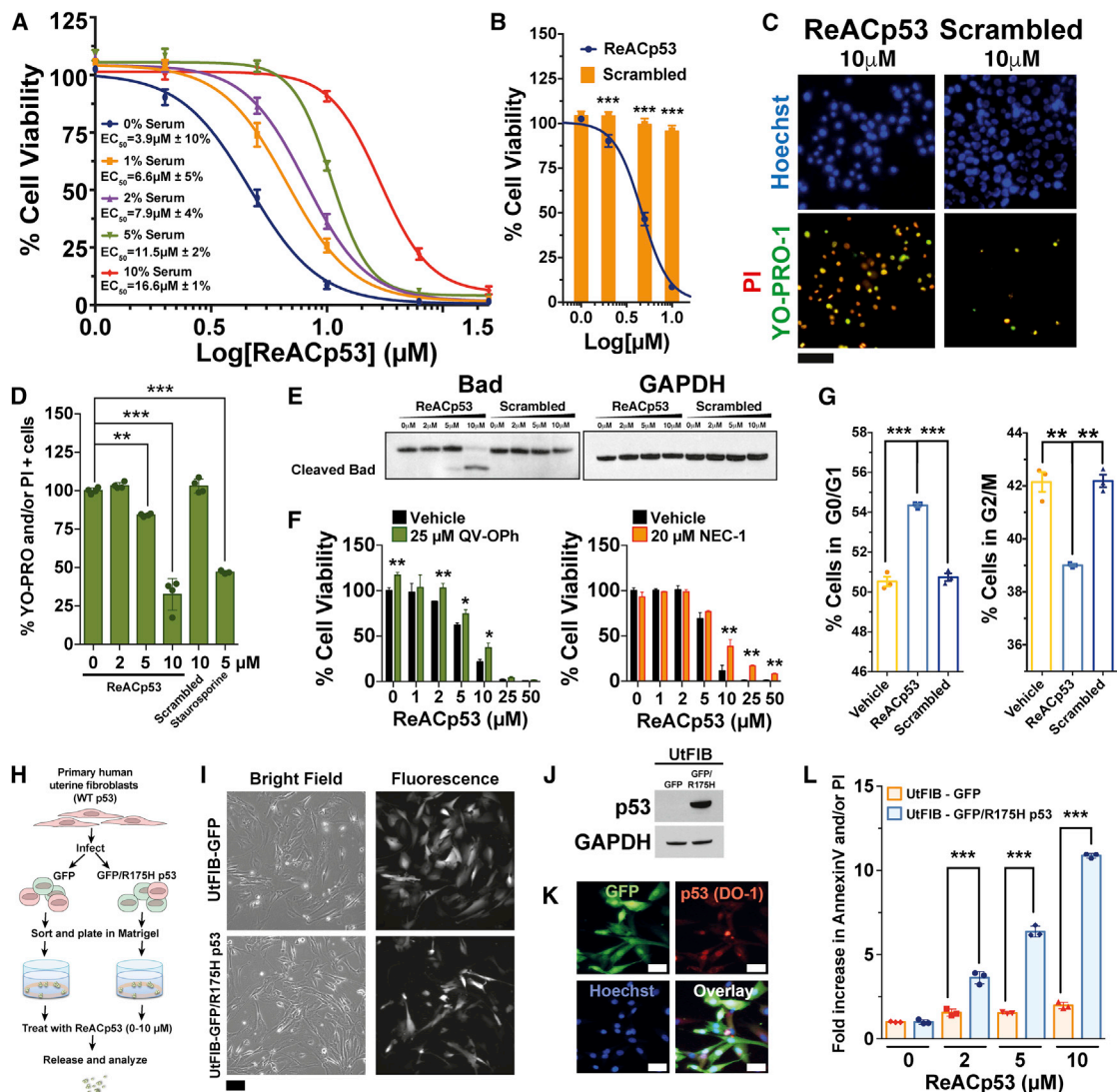


Figure 3. ReAcP53 Causes Cancer Cell Death

(A) 3-(4,5-dimethylthiazol-2-yl)-5-(3-carboxymethoxyphenyl)-2-(4-sulfophenyl)-2H-tetrazolium (MTS) assay shows a ReAcP53 concentration-dependent decrease in cell viability in S1 GODL cells. Values are represented as the average of six independent experiments ($n = 3/\text{experiment}$) \pm SEM. Average EC_{50} values from all experiments and their coefficient of variation are reported.

(B) A scrambled control peptide does not exhibit a significant effect. ReAcP53 is represented as the average of six independent experiments ($n = 3/\text{experiment}$) \pm SEM, scrambled is presented as average of three independent experiments ($n = 3/\text{experiment}$) \pm SEM. Means were compared with t tests, $***p < 0.0001$.

(C) ReAcP53-treated OVCAR3 cells stained with YO-PRO-1 and PI to label apoptotic and necrotic cells. A scrambled peptide control did not elicit significant cell death. Scale bar, 100 μm .

(D) YO-PRO-1/PI stain of S1 GODL cells treated for 16 hr as quantified by flow cytometry. Scrambled peptide and staurosporine were included as controls. Symbols represent biological replicates ($n = 2$) for two independent experiments, bars show the average for all experiments \pm SD. Statistical significance was calculated by performing a repeated measure ANOVA with Holm-Sidak's multiple comparison test, $**p < 0.001$, $***p < 0.0001$.

(E) Western blot showing Bad cleavage in S1 GODL cells upon treatment with ReAcP53 at concentrations of 5 μM and above, indicative of cell death. GAPDH stain was performed on the same membrane after stripping.

(F) MTS assay for ReAcP53/QV-OPh or NEC-1 co-treatments. Triplicates for each concentration were measured; one representative experiment out of $n = 4$ (QV-OPh) or $n = 3$ (NEC-1) is shown. ReAcP53-induced cell death could be partially rescued by inhibiting apoptosis with QV-OPh (at low ReAcP53 concentrations) or with NEC-1 (at high ReAcP53 concentrations). Averaged values normalized to vehicle are reported as $\% \pm$ SD. Means were compared with unpaired two-tailed t tests. $*p < 0.005$, $**p < 0.0005$.

(G) Cell-cycle distribution of S1 GODL cells treated with vehicle, 5 μM ReAcP53 or 5 μM scrambled peptide for 4/5 hr as evaluated by DNA content measured by flow cytometry. Symbols represent biological replicates ($n = 2$) for two independent experiments, bars show the average for all experiments \pm SEM. Statistical significance was calculated by performing a repeated measure ANOVA with Holm-Sidak's multiple comparison test, $**p < 0.001$, $***p < 0.0001$.

(H) Schematic of the UtFIB infection experiment.

(I) Bright field and green fluorescence of cells post-infection show GFP expression. Scale bar, 100 μm .

(legend continued on next page)

cytosolic, punctate staining with little nuclear p53 (Figures 2A, 2B, and S2A). This suggests that in these clinical samples grown as monolayers, mutant p53 mostly self-associates in the cytosol. After 16–20 hr of ReAcP53 treatment, the proportion of cells with p53 puncta was reduced to 5%–20%, and p53 could now be detected in the nucleus in 70%–100% of cells, depending on the patient (Figures 2A and 2B). The absence of aggregated cytosolic p53 together with the shift in localization suggests that p53 was disaggregated and possibly restored to a functional form. We confirmed this by staining a stable cell line we established from HGSC patient 1 (called S1 GODL; Janzen et al., 2015) with either DO-1 or PAb240 anti-p53 antibodies in the presence of increasing concentrations of ReAcP53. DO-1 recognizes any p53, regardless of conformation, while PAb240 is specific for partially unfolded p53. Because partially unfolded p53 is required for protein aggregation, we used PAb240 as a surrogate marker for aggregated p53. As visible in Figures 2C and 2D, there is less PAb240 binding upon ReAcP53 treatment, despite the presence of p53 in the cells as indicated by DO-1 staining, while the scrambled peptide control did not have any effect (Figure S2C). Immunoprecipitation with PAb240 using native lysates from vehicle- or ReAcP53-treated S1 GODL cells gave analogous results (Figure S2D). Collectively, these data indicate that the antigen recognized by PAb240 (residues 213–217, Figure 1B) is now buried in the protein core and no longer accessible.

ReAcP53 Induces Cancer Cell Death, Cell-Cycle Arrest, and Results in p53 Degradation

Next, we evaluated the effects of ReAcP53 on cell viability using OVCAR3 and S1 GODL cells. ReAcP53 reduced cell viability in a concentration-dependent manner, while a control sequence-scrambled ReAcP53 or the poly-arginine tag alone was ineffective (Figures 3A, 3B, and S3A). The peptide was also effective in the presence of increasing concentrations of serum (Figure 3A), albeit with lower effective concentration (EC_{50}) values. Consecutive daily treatments lowered the EC_{50} s even in the presence of as much as 10% serum (Figure S3B).

By light microscopy and transmission electron microscopy (TEM) (Figure S3C and S3D), mixed features of apoptotic/necrotic cell death were visible, such as nuclear envelope enlargement, isolated nuclear bodies, and condensed chromatin. As visible in Figure 3C, ReAcP53 increased the proportion of YO-PRO-1 (staining apoptotic cells) and propidium iodide (PI, staining late apoptotic/necrotic cells) OVCAR3-positive cells in a concentration-dependent manner, but a scrambled control peptide did not, strengthening the evidence for sequence specificity of ReAcP53. Similar results were obtained in S1 GODL cells (Figures 3D and S3E, quantified by flow cytometry). We could detect Bad cleavage after 16 hr of ReAcP53 treatment at concentrations of 5 μ M and above in S1 GODL cells (Figure 3E), indicative

of apoptosis. However, the pan-caspase inhibitor QV-OPH only partially rescued cell viability. NEC-1, an inhibitor of necroptosis, similarly showed a significant but incomplete rescue of cell viability (Figure 3F).

Another indication of rescued p53 activity is induction of G0/G1 cell-cycle arrest. To test this, we treated S1 GODL cells for 4/5 hr with ReAcP53 or a scrambled peptide and examined DNA content by flow cytometry. We detected a small but significant shift in the cell-cycle distribution of the asynchronous population, with more cells in G0/G1 and fewer in G2/M phase (Figure 3G). We observed a \sim 40% reduction in phospho-Rb(S608/611) consistent with a G0/G1 cell-cycle arrest in progress (Figures S3F and S3G). Levels of phospho-Chk2 were unaltered upon ReAcP53, suggesting that ReAcP53 does not induce DNA damage (Figure S3H).

Lastly, we checked for p53 levels upon ReAcP53 treatment. p53 cellular levels are tightly controlled to express little protein in the absence of a stimulus (Levine and Oren, 2009). This is due, at least in part, to MDM2, an ubiquitin ligase that targets p53 for proteosomal degradation. Partially unfolded p53 mutants typically cannot interact with MDM2, resulting in protein accumulation (Joerger and Fersht, 2008). In agreement with this hypothesis, we detected high levels of R248Q p53 in S1 GODL cells grown as a monolayer (Figure S3I). Upon ReAcP53 treatment, p53 levels gradually decreased. Given that there is less aggregated p53 upon ReAcP53 treatment (Figure 2D), we hypothesized that the wild-type (WT)-like folded protein could be interacting with MDM2. We used a pharmacologic approach to test this, by applying Nutlin-3, a p53-MDM2 interaction inhibitor, to S1 GODL cells treated with ReAcP53 (Vassilev et al., 2004). Upon combined ReAcP53/Nutlin-3 treatment, p53 levels were higher, supporting the idea that the now properly folded mutant p53 can interact with MDM2 (Figures S3J and S3K). Concurrent treatment with both molecules resulted in a synergistic reduction of EC_{50} values upon addition of 10 μ M Nutlin-3 in low passaged S1 GODL cells (Figures S3D–S3F).

ReAcP53 Induces Rapid Cell Death in Human Primary Uterine Fibroblasts Transfected with a Dominant-Negative R175H p53 Mutant Grown in 3D

To further validate p53 as the primary target of ReAcP53 action, we tested its effects on an isogenic background by infecting human primary uterine fibroblasts (UtFIB) with a GFP construct or a GFP/R175H p53-expressing construct (Figure 3H). GFP-positive fibroblasts were sorted and p53 expression was tested by western blot and immunofluorescence (Figures 3I–3K). The GFP/R175H p53-expressing UtFIB rapidly changed morphology and started proliferating faster than the GFP control (Figure 3I). In order to study the effects of ReAcP53 in a more physiological model system that better recapitulates drug responses observed in vivo, we tested UtFIB response to ReAcP53 using a 3D

(J) Western blot of lysates from GFP- and GFP/R175H p53-infected UtFIB showing p53 expression. GAPDH stain was performed on the same membrane after stripping.

(K) Immunofluorescence of fixed GFP/R175H p53-infected UtFIB showing p53 distribution in the cells. Scale bars, 50 μ m.

(L) Annexin V/PI staining of GFP- and GFP/R175H p53-infected UtFIB grown in 3D treated for 2 days with ReAcP53 as measured by flow cytometry. One representative experiment is shown ($n = 3$). Biological replicates (symbols, $n = 3$) are normalized to vehicle and expressed as fold change \pm SD. ANOVA with Tukey's honest significant difference significance criterion was performed to calculate p values. *** $p < 0.0001$.

See also Figure S3.

Matrigel culture system (L'Espérance et al., 2008). After seeding the cells in Matrigel and allowing them to grow for 2 days, GFP and GFP/R175H p53 UtFIB were treated twice with increasing ReAcP53 concentrations (0–10 μ M) and cell death was assessed by Annexin V/PI staining upon release from Matrigel (Figure 3L). The response to ReAcP53 in UtFIBs carrying the aggregating R175H p53 mutant was 2- to 10-fold higher than controls.

ReAcP53 Acts to Stabilize Mutant p53 In Vitro

Consistent with mutant p53 overexpression, we detected a significant amount of SDS-resistant p53 high molecular weight aggregates in GFP/R175H UtFIB (Figure S3O). We tested the effects of ReAcP53 on p53 stability by adding it to cell lysates of either normal untransfected UtFIB, GFP/R175H UtFIB, or S1 GODL (R248Q p53) lysates, followed by heating at 42°C for 10 min. This resulted in a high proportion of mutant p53 SDS-insoluble aggregates, which were significantly reduced by co-incubation with ReAcP53 (Figure S3O), indicative of a direct effect of ReAcP53 on p53 stability in vitro.

ReAcP53 Specifically Reduces Cell Viability and Proliferation of Cancer Cells Bearing Mutant but Not Wild-type p53 When Grown as Organoids

We established model organoids by growing S1 GODL cells for 2 days followed by two consecutive treatments with ReAcP53 (Figure 4A). We observed a reduction in cell viability reflected in the increased YO-PRO-1/PI staining (Figure 4B). Typically, S1 GODL organoids are 30–200 μ m in diameter, with central cavities filled with vesicles and pili (Figures S4A–S4C). Organoids treated for 2 days with 10 μ M ReAcP53 lose their morphology, with several cells being apoptotic/necrotic (Figures 4C and S4D–S4J). By TEM, we detected enlarged nuclear envelope and ER, chromatin condensation, and condensed mitochondria (Figures 4D and S4H–S4J), compatible with late apoptotic/necrotic cell death. Cell death was confirmed by Annexin V/PI staining of organoid cells derived from a panel of control cell lines (MCF7, SKOV3, Detroit562, S1 GODL, Table S4) and clinical samples from eight patients with different p53 status (Table S3) treated twice with ReAcP53. Results show extensive cell death in organoids bearing p53 aggregating mutations, but not WT or null cells (Figures 4E and S4K–S4M). Longer treatments (1 week) resulted in a higher proportion of HGSOc patient-derived organoids undergoing extensive cell death, with apparent EC₅₀ values in the low micromolar range (Figures 4F, S4N, and S4O). This was accompanied by a marked reduction in the number of Ki67 proliferating cells (Figure 4G). These results suggest that, in this clinically relevant model, ReAcP53 is effective on tumor cells bearing aggregation-prone p53 but not on WT folded protein or cells not expressing p53.

Transcriptional Reactivation of p53 by ReAcP53

The change in p53 protein conformation and localization, increased cell death, and reduction in proliferation are all compatible with rescued p53 function by ReAcP53. To gain further insights, we performed RNAseq of organoids generated from OVCAR3 cells and HGSOc patient 1 primary cells as well as MCF7 and primary cells derived from an ovarian endometrioid cancer patient (WT p53, patient 8) as controls, all treated for

2 days with 5 μ M ReAcP53 (Figure 5A). At a cutoff p value <0.01, over 2,400 transcripts were found to be differentially regulated 1.5-fold or more upon ReAcP53 treatment in the OVCAR3 sample, and over 700 for the HGSOc primary sample, with close to 80% overlap between datasets (Figure 5A). The definite differences upon ReAcP53 treatment in the two mutant p53 specimens resulted in segregation of treated and untreated samples in an unsupervised clustering. On the other hand, there were few differences in the control samples, so that treated and untreated were randomly clustered (Figure S5A). When examining the adjusted p value distribution, we found few transcripts with significant p values in the samples bearing WT p53 (Figure S5B). This suggests that ReAcP53 in the conditions tested does not have a significant effect on organoids generated from cells expressing WT p53, neither the cell line (MCF7) nor the primary endometrioid tumor from patient 8, while eliciting a clear effect at the transcriptional level for cells carrying the aggregating R248Q mutation.

Ingenuity pathway analysis (IPA) revealed that the majority of differentially regulated transcripts were related to cellular growth and proliferation, movement, death and survival, and cellular development for both OVCAR3 and HGSOc patient 1 samples (Figures 5B and S6C). Gene ontology analysis of the OVCAR3 dataset highlighted that the most represented terms in the upregulated mRNAs were regulation of transcription and RNA metabolic processes, regulation of cell proliferation, and cell death, while the downregulated mRNAs were related to oxidation reduction, response to organic substance and cell adhesion, and generation of metabolites and energy (Figure S5D). Upstream regulator analysis of the OVCAR3 dataset performed by IPA revealed how p53 was the most significant upstream transcriptional regulator (Table S5), strengthening the idea that ReAcP53 acts on p53. We selected ~80 transcripts, which are known either as p53 transcriptional targets or as part of the p53 signaling network, and mapped their expression levels for vehicle- and ReAcP53-treated organoids (Figures 5C and S5E). Among the upregulated mRNAs are some well-characterized p53 targets such as p21, GADD45B, PUMA, THBS1, NOXA, and DRAM1. Significant fold changes for these were found in the responsive tumor sample and OVCAR3 cells only (Figure 5D). Two p53 homologs, p63 and p73, were differentially regulated, with p63 being upregulated and p73 being downregulated also at the protein level in both OVCAR and S1 GODL cells (Figures 5D–5F). Besides the p53 network, we identified several metabolic processes that are affected by ReAcP53. Among these, glycolysis and gluconeogenesis, citrate cycle, pyruvate, lipids and nicotinamide metabolism, and the mevalonate pathway were downregulated (Figure S5F). The last is of particular interest given that it has been shown to be upregulated by mutant p53 (Freed-Pastor et al., 2012).

ReAcP53 Detection and Pharmacokinetics Profile in Serum of Treated Animals

Next we checked in vivo stability and resistance to proteolytic cleavage, which are potential challenges for ReAcP53 administration. To do so, we determined the in vivo pharmacokinetics profile of ReAcP53. Given that ReAcP53 is a peptide, its unambiguous detection in complex mixtures such as serum required the optimization of a sensitive liquid chromatographic/tandem

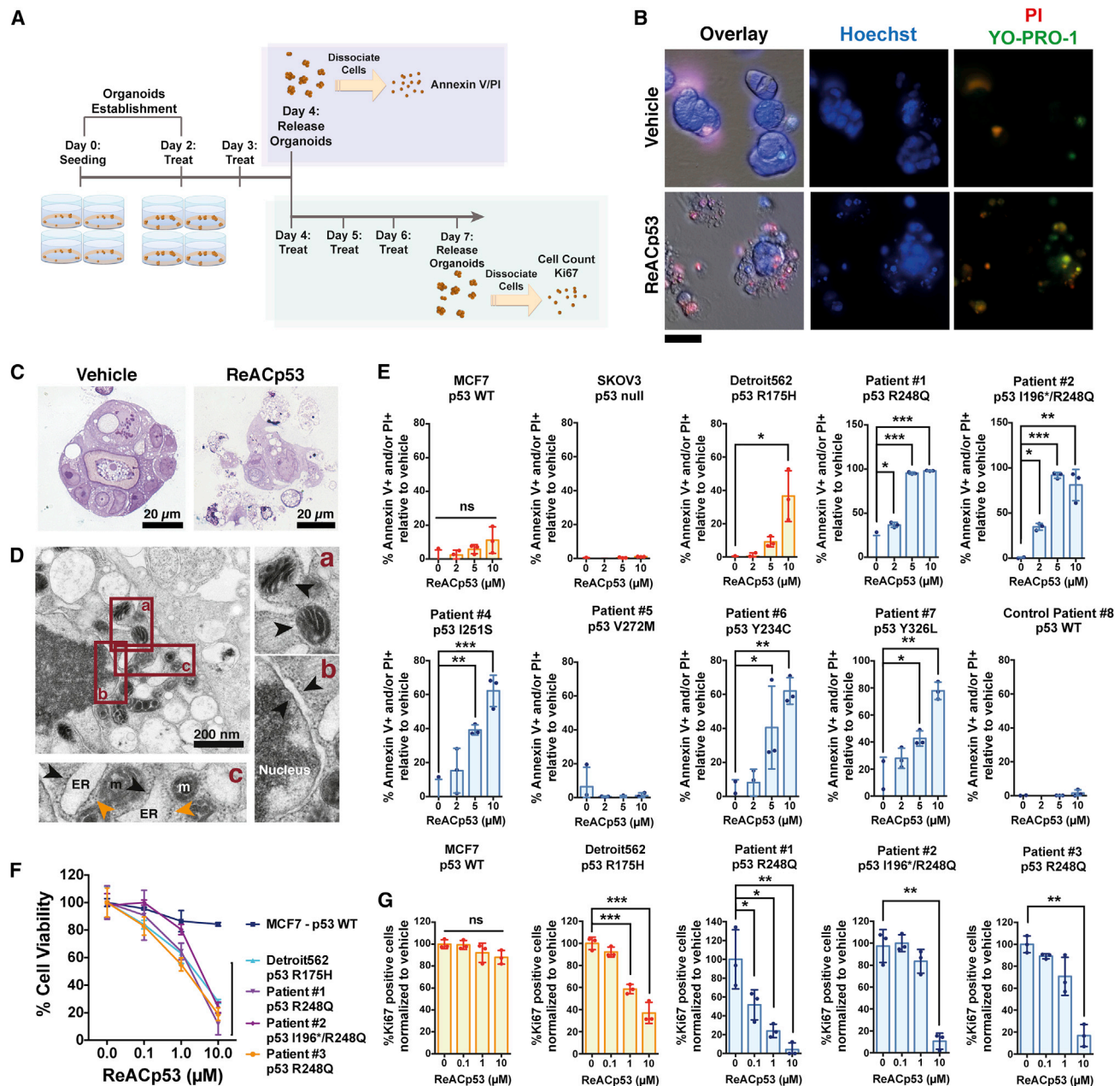


Figure 4. ReAcP53 Causes Cell Death in Organoids Generated from HGSOC Samples Bearing p53 Mutations

(A) Schematics of the experiments performed in the 3D organoid model system. The blue and green boxes represent the two different types of experiment performed. (B) S1 GODL organoids treated with 10 μ M ReAcP53 undergo a dramatic change in cell morphology and internalization of YO-PRO-1/PI, indicative of cell death. Scale bar, 50 μ m.

(C) Semi-thin sections of the organoids show the catastrophic effect of ReAcP53 on their morphology.

(D) TEM analysis of the same sample shows several features of apoptotic cells, including condensed mitochondria (a), an enlarged nuclear envelope (b), and enlarged ER (c, black arrowheads) and free ribosomes (orange arrowheads).

(E) ReAcP53 affects the cell viability of organoids generated from cell lines or HGSOC primary samples bearing p53 mutations. Organoids were treated for 2 days with the indicated ReAcP53 concentrations and Annexin V/PI staining was measured by flow cytometry. Symbols are individual replicates ($n = 3$), bars are averages \pm SD; one representative experiment shown ($n \geq 2$). p values were calculated by repeated measure ANOVA with Holm-Sidak's multiple comparison test * $p < 0.05$, ** $p < 0.005$, *** $p < 0.0001$.

(F) Cell viability determined after a week of daily ReAcP53 treatments by cell counting of triplicate samples. Values are normalized to vehicle; symbols show the average of triplicates \pm SD.

(G) ReAcP53 induces a significant decline in % of Ki67 positive cells relative to vehicle after a 1-week treatment course as quantified by intracellular Ki67 levels measured by flow cytometry. Symbols represents individual replicates, bars are average values \pm SD. Statistics calculated as in (E) * $p < 0.05$, ** $p < 0.005$, *** $p < 0.0001$.

See also Figure S4.

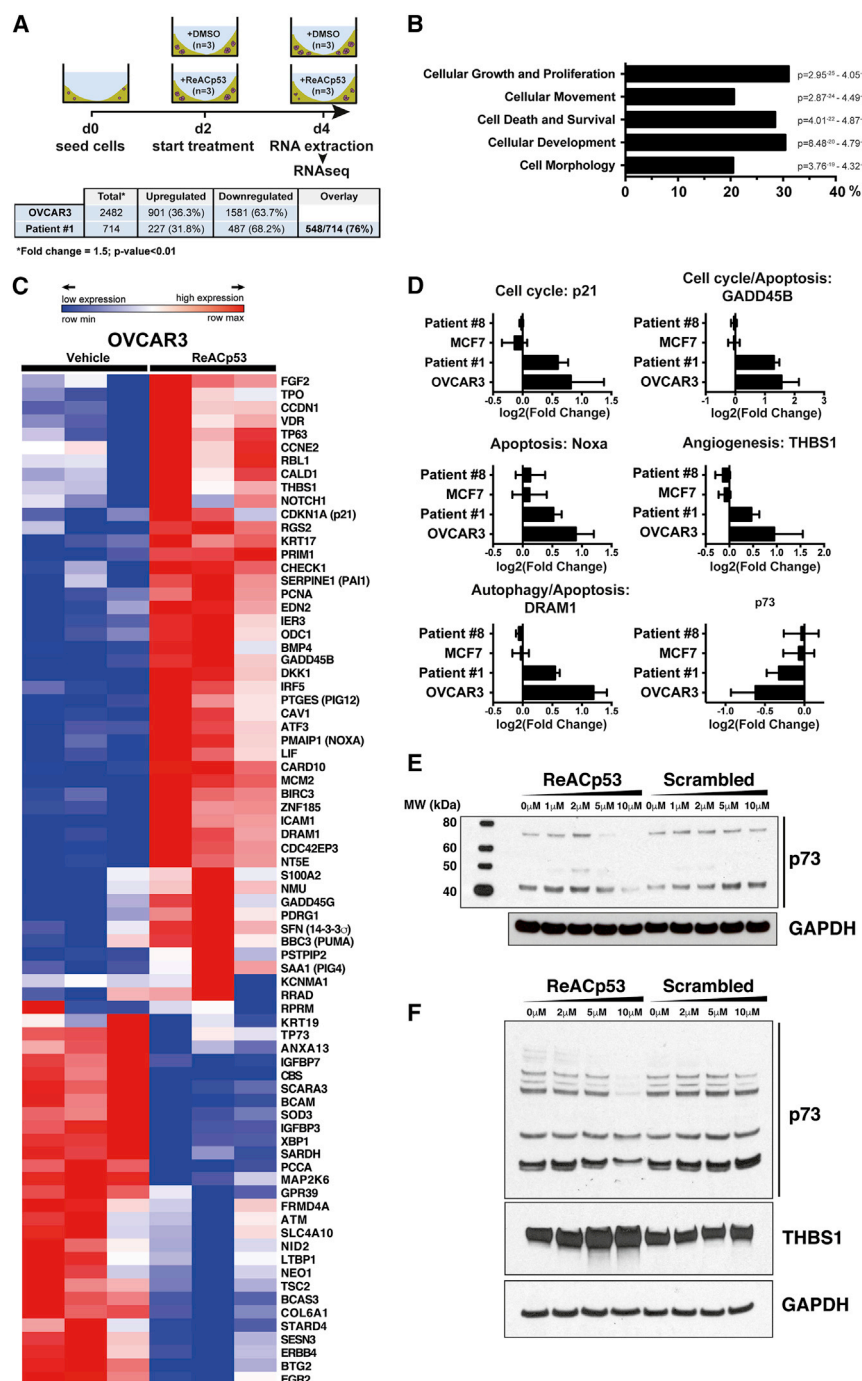


Figure 5. RNAseq of ReAcP53-Treated Organoids

(A) Scheme of experimental setup and overview of results.

(B) IPA analysis of molecular functions for the OVCAR3 dataset.

(C) Heatmap of a subset of p53 pathway genes differentially regulated in ReAcP53-responsive OVCAR3 organoids. Several canonical p53 targets are present.

(D) Fold change for a subset of p53 transcriptional targets. Data are shown as \log_2 (fold change); bars represent the average of three replicates \pm SD.

(E) OVCAR3 cells have less p73 protein upon ReAcP53 exposure as visualized by western blot.

(F) p73 reduction and thrombospondin increase at the protein level in S1 GODL cells correlates with the mRNA levels. In all cases, GAPDH stain was performed on the same membrane after stripping. All blots were repeated three times on three independent cell lysates. One representative example is shown.

See also Table S5 and Figure S5.

ReAcP53 serum peak concentration was still present in the circulation after 24 hr, although we cannot unambiguously determine whether the peptide detected was intact or partially proteolyzed due to the trypsin treatment that is part of the sample preparation procedure (see [Supplemental Experimental Procedures](#)). Nevertheless, the high stability of ReAcP53 warranted further in vivo testing.

In Vivo Administration of ReAcP53 Results in Reduced Tumor Proliferation and Shrinkage in Two HGSOC Xenograft Models

In the minimal residual disease model, three cohorts of mice ($n = 3$) were injected with a Matrigel/OVCAR3 (p53 mutant) suspension on one flank and with a Matrigel/MCF7 (WT p53) suspension on the other flank in order to provide an internal control for specificity of ReAcP53 to preferentially target mutated aggregation-prone p53. Treatment was started the same day (Figure 6A). In the treatment protocol, tumors were allowed

mass spectrometric assay called multiple reaction monitoring (MRM; see [Supplemental Experimental Procedures](#) for details) (Anderson and Hunter, 2006). The assay allowed us to discriminate ReAcP53 with high specificity in both serum and tissues.

ReAcP53 administered intraperitoneally quickly entered the systemic circulation and could be detected in the serum of treated immunocompromised mice with a peak concentration of $1.2 \pm 0.3 \mu\text{M}$ at the 1-hr time point (Figures S6A–S6C). In addition, we could detect ReAcP53 in tumor tissue (Figure S6D). While the apparent half-life in serum was ~ 1.45 hr, close to 20% of the

to develop for 2 weeks prior to treatment initiation (Figure 6A). In both models, the treatment phase consisted of 3 weeks of daily intraperitoneal (IP) injections with 15 mg/kg of ReAcP53, sequence-scrambled control peptide, or vehicle alone. The intraperitoneal route was chosen as IP administration of chemotherapeutic drugs in ovarian cancer patients has been shown to be more efficacious than systemic administration and has been recommended by the National Cancer Institute for existing standard treatments (Morgan et al., 2013). For both models, tumor volumes monitored daily indicated that

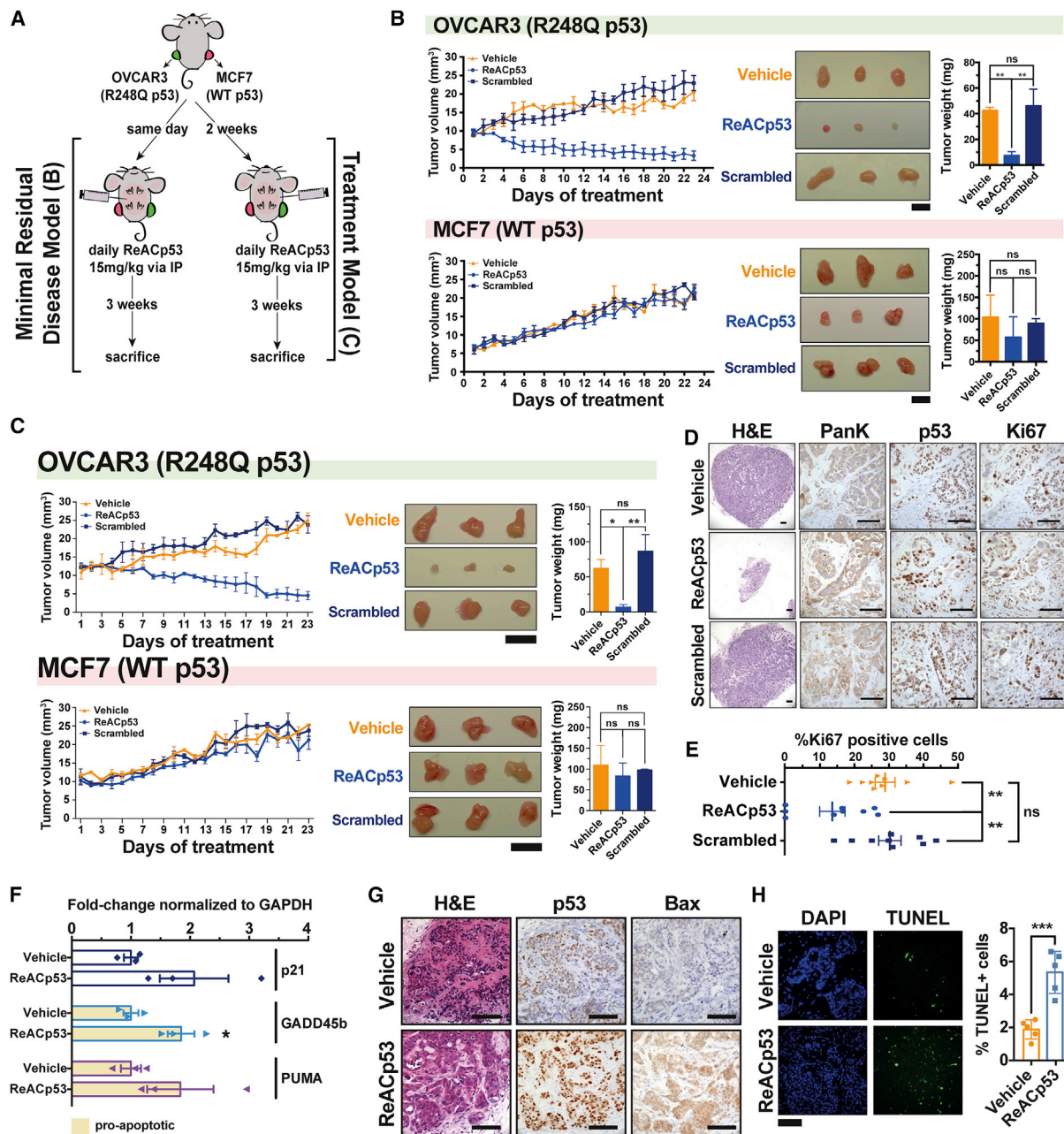


Figure 6. ReAcP53 Causes Regression of Xenografts Bearing an Aggregation-Prone p53 Mutant In Vivo

(A) Schematics of the experimental design for xenograft models. Both in vivo experiments were performed twice, with $n = 3$ mice/group, one representative experiment is shown.

(B) Minimal residual disease model. Tumor growth monitored over time showed a reduction in size of OVCAR3 but not MCF7 xenografts in mice treated with ReAcP53. Data are shown as average volumes (symbols, $n = 3$) \pm SEM. Means of tumor weights ($n = 3$) are shown as averages (bars) \pm SD and compared using an ANOVA model and Tukey's honest significant difference significance criterion. ** $p < 0.05$. Scale bars, 1 cm.

(C–H) Treatment model. Scale bars, 1 cm. (C) Same as in (B) * $p < 0.05$, ** $p < 0.005$.

(D) H&E and IHC on residual xenografts. Sections were stained for PanK, p53, and Ki67. Scale bars, 50 μ m.

(E) Total and Ki67-positive cells were quantified on three different fields for each xenograft, and reported as % Ki67 positive cells (symbols). Lines represent the average for each treatment group \pm SEM. p values were calculated by ANOVA using the Tukey honest significant difference significance criterion. ** $p < 0.01$.

(F) qPCR analysis of residual S1 GODL xenografts treated with 30 mg/kg ReAcP53 for 9 days. Symbols represents the fold change normalized to GAPDH for $n = 3$ xenografts, bars are average values \pm SEM. * $p < 0.05$.

(G) H&E and IHC on short-term treated xenografts show abundant Bax expression, indicative of apoptosis. Scale bar, 100 μ m.

(H) TUNEL assay also showed a significantly higher proportion of cell deaths in ReAcP53-treated grafts. Symbols represent the % of TUNEL-positive cells in five fields of view sampling all the tumors, while bars show the average values \pm SD, *** $p < 0.0001$. Scale bar, 100 μ m.

See also Table S6 and Figure S6.

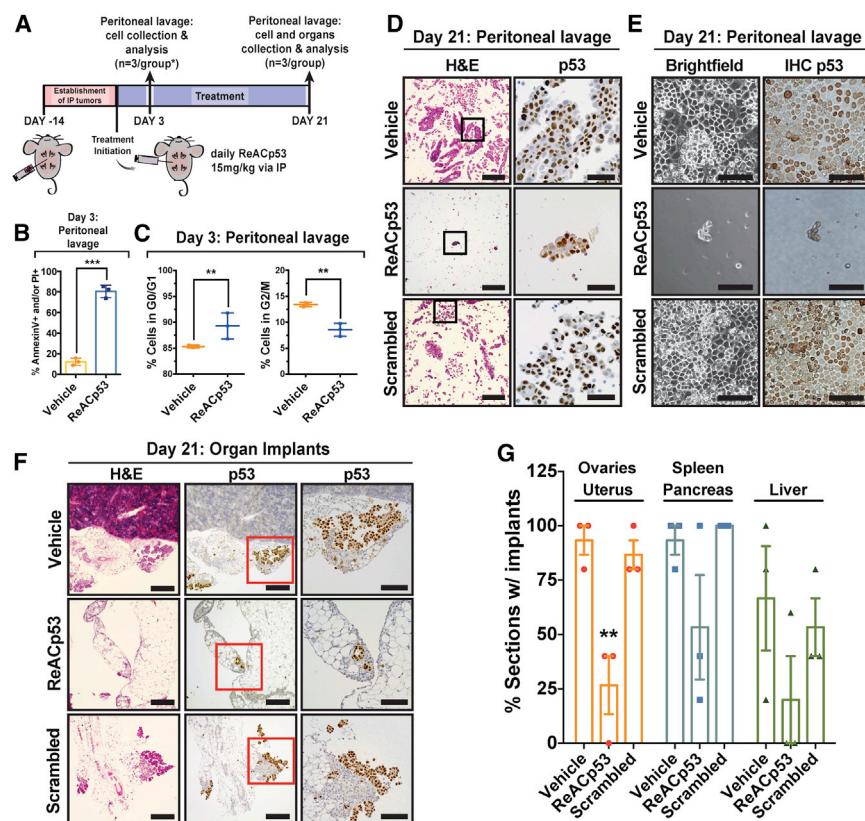


Figure 7. ReACp53 Causes Regression of Intraperitoneal Disseminated Tumors In Vivo

(A) Schematics of the IP disseminated disease model experiment.

(B) Viability of cancer cells obtained from ascites (discussed in the Experimental Procedures) after four daily treatments as measured by flow cytometry of Annexin V/PI stained cells. Symbols represent values from individual mice (n = 3/group), bars are average \pm SD. Means were compared by t test. ***p < 0.001.

(C) Cell-cycle distribution of tumor cells obtained from ascites as measured by flow cytometry. Symbols represent values from individual mice (n = 3/group), lines are averages \pm SD. Means were compared by t test. **p < 0.01.

(D) Analysis of pelleted ascites-derived cancer cells by H&E and IHC. The black boxed area is magnified on the right. Scale bars, 200 μ m for H&E; 50 μ m for IHC.

(E) Bright field and IHC of cancer cells obtained from ascites after a 3-week treatment and plated to confirm viability. Quadruplicates were plated for each mouse (n = 3 mice/group). The ReACp53-treated samples did not yield any live and proliferating cell. Scale bars, 100 μ m.

(F) Organ implants as visualized by H&E and identified by positive p53 IHC staining. Scale bars, 200 μ m for H&E and low magnification IHC; 50 μ m for high magnification IHC.

(G) Quantification of organ implants upon histological examination of p53 stained sections. This conservative analysis does not take into account

implant size, which was typically small (3–5 cells) in ReACp53-treated samples. Each symbol represents the average for all sampled sections (n = 5) for a given mouse; three mice are reported. Bars represent averages for the three mice \pm SEM. A statistically significant difference in the presence of implants in the uterus/ovaries was detected by performing repeated measure ANOVA with Holm-Sidak's multiple comparison tests. **p < 0.05. Scale bars, 200 μ m for H&E; 50 μ m for IHC.

only OVCAR3 xenografts treated with ReACp53 shrank while both vehicle- and scrambled control-treated tumors more than doubled in size (Figures 6B and 6C). Mutant p53-bearing tumors in the ReACp53-treated mice cohorts were 80%–90% smaller in weight than the control cohort (Figures 6B and 6C), confirming the ability of ReACp53 to limit tumor proliferation and shrink tumors in vivo. Analysis of residual tumors from the treatment model by Hematoxylin and eosin (H&E) stain showed a higher ratio of Matrigel to tumor cells for ReACp53-treated xenografts (Figure 6D). Tumor sections were stained with PanK (marking tumor epithelia), p53, and Ki67 (Figure 6D). A significant reduction of Ki67-positive cells was evident in ReACp53-treated OVCAR3 xenografts, indicative of a reduced proliferative index (Figures 6E, S6I, and S6J). MCF7 xenografts carrying WT p53 were not responsive (Figure 6C) indicating that, at least in this experimental design, tumors harboring a functional WT p53 are unaffected by ReACp53. Similar results were observed in the minimal residual disease model (Figures S6G–S6J). In this paradigm, administration of ReACp53 resulted in a significant increase in p21 and MDM2 transcription in OVCAR3 but not MCF7 xenografts (Figure S6K).

Piknotic nuclei and scarcity of mitotic figures were evident in the residual grafts, suggestive of extensive cell death and reduced proliferation (Figure S6E). We confirmed this in an independent experiment using pre-established xenografts gener-

ated from patient-derived stabilized cells (S1 GODL) treated with either vehicle or ReACp53 for 9 days. mRNA levels for a selection of p53 targets including the pro-apoptotic GADD45b and PUMA were increased in the ReACp53-treated grafts (Figure 6F). Immunohistochemistry (IHC) analysis revealed a significant increase in Bax protein levels (Figure 6G). In addition, we performed a TUNEL (terminal deoxynucleotidyl transferase dUTP nick end labeling) assay and observed a significantly increased number of dying cells in the ReACp53 implants (Figure 6H). These results confirm that ReACp53 not only induces proliferative arrest but also cell death in xenografts bearing mutant p53 in vivo.

In Vivo Administration of ReACp53 in a Physiological Intraperitoneal Disseminated Disease Model Causes Cell Death and Reduction of Organ Implants

To confirm the therapeutic relevance of ReACp53, we shifted toward a more relevant in vivo model by injecting 2.5×10^6 HGSOc patient-derived cells (S1 GODL) intraperitoneally. Organ tumor implants and ascites developed over a 2-week period and were confirmed histologically before initiation of therapy (Figure 7A). Three mice from the vehicle- and ReACp53-treated cohorts were sacrificed after four daily IP treatments and ascites were analyzed. Over 80% of cells were Annexin V and/or PI positive in the ReACp53 group (Figure 7B).

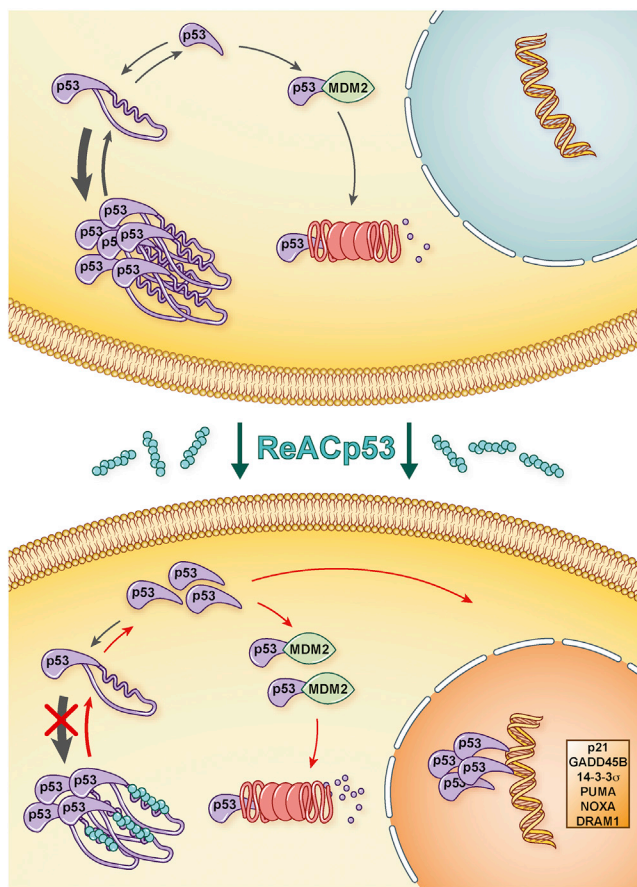


Figure 8. Model for the Mechanism of Action of ReACp53

Unstable p53 mutants partially unfold, exposing the aggregation-prone segment LTIITL. This segment interacts with the same segment from other p53 molecules, driving p53 into its inactive aggregated state (top). ReACp53 (cyan) treatment blocks the aggregation pathway, shifting the equilibrium toward functional, soluble p53 (bottom). Functional p53 enters the nucleus and induces cell death and proliferation arrest. Folded p53 interacts with MDM2 and is degraded.

We also found a significantly increased population in G0/G1 phase (Figure 7C), supporting proliferative arrest upon ReACp53 administration *in vivo*. After the 3 weeks of daily IP treatments, mice were sacrificed and ascites and organs were analyzed. An equal small aliquot of cells derived from the IP cavity by peritoneal lavage were plated in quadruplicate. Only the vehicle- and scrambled-treated cells grew in culture (Figure 7D). The remaining tumor cells from the peritoneal lavage were pelleted, fixed, and embedded for histological analysis. This analysis confirmed that the ReACp53-treated mice had very few residual tumor cells in the peritoneal cavity compared with vehicle- or scrambled-treated controls (Figure 7E). Similarly, organ implants were less frequent and composed of fewer cells in the ReACp53 mice (Figures 7F and 7G).

ReACp53 Is Well Tolerated *In Vivo*

We monitored the treated mice for possible side effects arising from the administration of ReACp53. Complete cell blood counts

and ions, total proteins, and kidney and liver function were assayed. As shown in Table S6, we did not detect any significant alteration of values upon ReACp53 treatment compared with vehicle-treated mice. The anatomy of major organs was unaltered, with no difference between ReACp53-, vehicle-, or scrambled peptide-treated samples (Figure S6M). These results suggest that, at the dose studied, ReACp53 is well tolerated and does not induce measurable toxicities.

DISCUSSION

Folded, partially unfolded, and aggregated p53 are in equilibrium (Bullock and Fersht, 2001). p53 aggregation is a highly favored process in those instances where a structural mutation destabilizes the molecule permitting exposure of the adhesive segment p53_{252–258} that is normally buried deep within the protein (Bullock et al., 1997; Bullock and Fersht, 2001; Xu et al., 2011). Previous efforts to rescue p53 function have focused on stabilizing the native fold by chemical modifications or ligand binding, shifting the equilibrium toward the active conformation. This approach has been successful *in vitro* (Bykov et al., 2002; Issaeva et al., 2003; Liu et al., 2013; Wilcken et al., 2012; Yu et al., 2012) with one molecule advancing to the clinical phase (APR-246; Lehmann et al., 2012; Khoo et al., 2014). The purpose of ReACp53 is also to rescue p53 function, but it acts at a different step of the dynamic equilibrium: p53 aggregation. Once exposed, the adhesive segment 252–258 binds to identical segments in other destabilized p53 molecules. ReACp53 is designed to mask this segment in the aggregates, preventing further aggregation and shifting the folding equilibrium toward its functional, WT-like state (Figure 8). Consistent with this mode of action, when HGSOc patient-derived primary cells are treated with ReACp53, neither unfolded nor aggregated p53 are observed. Rather, the aggregation-prone mutant p53 seen in untreated cells in punctate form in the clinical samples examined is dispersed and relocalized to the nucleus.

When culturing tumor cells as organoids in a physiologically relevant 3D system, we observe that ReACp53-rescued p53 behaves similarly to the WT counterpart by inducing cell death and cell-cycle arrest. In the tumor organoids, these effects were observed only in those specimens bearing mutant but not WT p53 protein. In further support of the conversion of p53 in treated cells from aggregated to functional states, we observed by RNA-seq that several p53 target genes in organoids generated from OVCAR3 cells bearing R248Q p53 are differentially regulated, including upregulation of canonical p53 targets such as PUMA, NOXA, p21, GADD45B, and 14-3-3σ.

Our data on this particular set of samples are consistent with the observation that restoring the oncosuppressive function of WT p53 leads to tumor regression (Ventura et al., 2007). On the other hand, mutant p53 is a bona fide oncogene. It has been shown that some tumor cells expressing gain-of-function mutants of p53 are addicted to its expression (Muller and Vousden, 2013). As such, given that p53 levels decrease upon ReACp53 treatment, some of the effects observed might be linked to removal of a crucial oncogene. This could potentially be mutation and/or context dependent (Vaughan et al., 2012). In cells where this process is dominant, one could expect Nutlin to antagonize the effects of ReACp53.

Consistent with the loss of the gain-of-function phenotypes exhibited by mutant p53 is the observation that genes known to be upregulated by mutant p53 were downregulated upon ReACp53 exposure. As an example, we found that most genes in the mevalonate pathway were downregulated. This pathway contributes to cell migration and invasion in ovarian cancer (Hashimoto et al., 2005) and is activated through interaction of mutant p53 with SREBP transcription factors (Freed-Pastor et al., 2012). Blocking the mevalonate pathway in HGSOc has been shown to be beneficial, given that compounds such as alendronate, lovastatin, fluvastatin, and zoledronic acid reduce the tumor burden and presence of ascites in vivo, and tumor invasion in vitro and in vivo (Hashimoto et al., 2005; Knight et al., 2009; Martirosyan et al., 2010).

Besides the mevalonate pathway, several other metabolic processes are impacted by p53 through various mechanisms (Kruiswijk et al., 2015). ReACp53 treatment resulted in lower mRNA levels for enzymes involved in the tricarboxylic acid cycle, oxidative phosphorylation, pyruvate and nicotinamide metabolism, glycolysis, and gluconeogenesis. This reduction in glycolytic metabolism may result in lower glucose uptake, suggesting the possibility of using fluorodeoxyglucose-positron emission tomography (FDG-PET) to detect early response to ReACp53 in vivo.

While several of the effects of ReACp53 at the transcriptional level are in anticipated directions, some variations were unexpected. One might expect p73 mRNA levels to increase upon p53 activation (Vossio et al., 2002), but our RNAseq data showed a reduction, also reflected at the protein level. Relevant to this finding, p73 is increased at both mRNA and protein levels in over 70% of ovarian cancers (Rufini et al., 2011), and its overexpression has been associated with high-grade malignancies (Chen et al., 2000). It was reported that p53 inactivation might cause p73 upregulation through E2F (Tophkhane et al., 2012), although other mechanisms such as direct p73 sequestration through co-aggregation are possible (Xu et al., 2011). Nevertheless, p53 reactivation by ReACp53 in our system is accompanied by a reduction in p73 levels, a potential beneficial effect in ovarian cancer. In summary, directionality of some of the changes we observed by RNAseq may be relevant and beneficial to the specific disease setting.

Arresting p53 aberrant self-aggregation could also block its co-aggregation with other proteins, which, upon ReACp53 administration, can resume their functions and contribute to the effects seen. In particular, p63 and p73 have been shown to co-aggregate with mutant p53 (Xu et al., 2011). Alternatively, p63 and p73 might be direct ReACp53 targets as they both have segments with high similarity to the p53 aggregation-prone sequence (Xu et al., 2011). Whether these or other proteins are targeted by ReACp53 remains to be evaluated.

To characterize ReACp53 effects in vivo, we tested it on two xenograft models obtaining an 80%–90% reduction in tumor burden depending on the paradigm. For these experiments, ReACp53 was administered via IP, a standard route of administration of drugs for the HGSOc patient population. Of note, we observed therapeutic efficacy at distant tumor sites in vivo. This is consistent with the favorable stability of ReACp53 in serum, as judged by its pharmacokinetics profile. In addition, efficacy was proven in a physiological disseminated disease

model that faithfully recapitulates the HGSOc characteristics observed in patients, including the presence of ascites and implants in distant organs including liver, omentum, and spleen (Naora and Montell, 2005). Standard blood tests and detailed necropsies revealed no tissue damage or blood alterations, supporting the non-toxic behavior of this peptide.

The usefulness of ReACp53 in cancer treatment may be in co-administration with carboplatin. The current standard of care for HGSOc patients entails platinum-based chemotherapy, with superior effects when administered intraperitoneally (Morgan et al., 2013). Carboplatin generates DNA damage, which in turn activates the p53 pathway driving cell death, provided that p53 is functional (Siddik, 2003). Given that p53 is frequently mutated and not functional in HGSOc, combining an agent that restores p53 functionality such as ReACp53 with carboplatin therapy may be a valuable therapeutic option that warrants further exploration.

ReACp53 may be effective in treating various cancer types. In principle, it could be useful in all tumors where p53 inactivation arises through partial unfolding and aggregation. With thousands of different p53 mutations described (IARC TP53 database, <http://p53.iarc.fr>) (Petitjean et al., 2007), we cannot yet anticipate which will respond to ReACp53, other than the well-established aggregation-prone mutations. We showed here that we can target two of the three most common p53 hotspot mutations in HGSOc (R175 and R248), which account for >15% of all cases of ovarian cancer (IARC TP53 database, <http://p53.iarc.fr>) (Petitjean et al., 2007). An additional feature is that ReACp53 should have no effect on cells with folded WT p53. We did not observe significant effects of ReACp53 on WT p53-carrying cells in the organoid 3D assays or in vivo. However, ReACp53 may also affect tumors bearing WT p53 if the protein is partially unfolded and aggregated. WT p53 has been reported in a mutant-like, aggregated conformation in basal cell carcinoma and hypoxic tumors (Lasagna-Reeves et al., 2013; Rieber and Strasberg-Rieber, 2012) and therefore could potentially be targeted by ReACp53 in specific cases.

In conclusion, the work presented here supports treating susceptible cancers as protein aggregation diseases as an alternative approach to cancer therapy.

EXPERIMENTAL PROCEDURES

Cell Lines and Clinical Samples

This study was approved by the UCLA Office for the Protection of Research Subjects (IRB 10-000727). High-grade serous cancers, obtained from consenting patients, were dissociated to single cells by enzymatic digestion. The S1 GODL cell line was established from primary cells derived from patient 1's tumor. The detailed procedure for the derivation and characterization of S1 GODL will be described elsewhere (Janzen et al., 2015). Cell lines were obtained from ATCC, maintained in an 8% CO₂ incubator at 37°C and used within 15 passages. All the cells used in this study were propagated in the ATCC-recommended serum supplemented medium and treated in serum-free medium (PrEGM, Lonza).

In Vitro 3D Organoid Assay

Single-cell suspensions (20,000 cells/well) were plated around the rim of a 24-well cell culture dish in a 1:1.3 mixture of PrEGM medium (Lonza CC-3166) and Matrigel (BD Biosciences), and overlaid with 500 μ l of PrEGM. Two days after plating, treatment with ReACp53, scramble peptide, or vehicle (DMSO) was initiated. A complete medium change was performed daily. Following

treatment (day 2 or day 7, depending on the experiment), HGSOc organoids were released from Matrigel by incubation in 1 mg/ml dispase (Invitrogen). Organoids were incubated in warm 0.05% Trypsin-EDTA, then passed through a 20-gauge syringe to yield single cells. Cell viability was determined by manual cell count. Apoptosis and proliferation were determined by flow cytometry (BD LSR II flow cytometer) of cells after staining. For each sample, 0.5 μ l of AnnexinV-FITC and 2 μ l of 50 μ g/ml PI (BD Biosciences) diluted in 1 \times Annexin binding buffer were added to cells according to the manufacturer's instructions. Ki67 (Vector Laboratories) was used at 0.5 μ l/sample on fixed cells in PBS. For reporting, results were normalized to vehicle-treated controls.

Animal Experiments

All animal experiments were approved by the UCLA Animal Research Committee and performed under oversight of the Division of Laboratory Animal Medicine (DLAM). Immunocompromised NSG mice (Jackson Laboratories: NOD.Cg-Prkdc^{scid}/J2rg^{tm1Wjl}/SzJ) were housed on a 12-hr light/dark schedule.

ACCESSION NUMBERS

The RCSB PDB accession numbers for the X-ray atomic resolution structures of the p53 amyloid segments 252–258 and 253–258 are PDB: 4RP6 and 4RP7, respectively. The NCBI Gene Expression Omnibus accession number to download the RNAseq data is GEO: GSE74550.

SUPPLEMENTAL INFORMATION

Supplemental Information includes Supplemental Experimental Procedures, six figures, and six tables and can be found with this article online at <http://dx.doi.org/10.1016/j.ccell.2015.12.002>.

ACKNOWLEDGMENTS

We thank Dr. Gregory Lawson for assisting with histological examination of tissues and Dr. Jiaoti Huang for sharing the lentiviral GFP/R175H p53 construct; Dr. Stuart Sievers and Jung-Reem Woo for support with the initial p53 structural characterization; Marco Morselli, Arturo Rinaldi and Dr. Ludmilla Rubbi for help with preparation of the libraries; Dr. Hans-Uwe Simon for helpful discussions. We acknowledge the support of Austin Quach and Farbod Fazlollahi with the MRM assay; the Pasarow Mass Spectrometry Laboratory is supported by NIH grant 1S10RR023718-01A2. This work was supported by grants from the Pardee Foundation (to A.S.), the NIH (AG-029430 to D.S.E.; R01CA183877 to S.M.), the NIH/National Center for Advancing Translational Science UCLA CTSI Grant UL1TR000124 (to A.S. and D.S.E.), the American Cancer Society (RSG-14-217-01-TBG to S.M.), the National Science Foundation (MCB 0958111, to D.S.E.), the Jonsson Cancer Center Foundation/UCLA (to S.M. and D.S.E.); the Lynne Cohen Foundation, the Phase One Foundation, the Ovarian Cancer Circle Inspired by Robin Babbini, the Leath L. and Marcia L. Millen Family Fund and the G.O. Discovery Lab Foundation (to S.M.), the HHMI (to D.S.E.) and in part by a VA CDA-2 award (1 K12 BX 001305-01 to S.M.). A.S., L.J. and D.S.E. are inventors on a patent application based on ReAcP53 (WO2014182961 A1). A.S. is a consultant for ADRx, Inc.; D.S.E. is a founder, head of the scientific advisory board and equity holder of ADRx, Inc.

Received: February 2, 2015

Revised: June 24, 2015

Accepted: December 9, 2015

Published: December 31, 2015

REFERENCES

Ahmed, A.A., Etemadmoghadam, D., Temple, J., Lynch, A.G., Riad, M., Sharma, R., Stewart, C., Fereday, S., Caldas, C., Defazio, A., et al. (2010). Driver mutations in TP53 are ubiquitous in high grade serous carcinoma of the ovary. *J. Pathol.* 221, 49–56.

Anderson, L., and Hunter, C.L. (2006). Quantitative mass spectrometric multiple reaction monitoring assays for major plasma proteins. *Mol. Cell Proteomics* 5, 573–588.

Bullock, A.N., and Fersht, A.R. (2001). Rescuing the function of mutant p53. *Nat. Rev. Cancer* 1, 68–76.

Bullock, A.N., Henckel, J., DeDecker, B.S., Johnson, C.M., Nikolova, P.V., Proctor, M.R., Lane, D.P., and Fersht, A.R. (1997). Thermodynamic stability of wild-type and mutant p53 core domain. *Proc. Natl. Acad. Sci. USA* 94, 14338–14342.

Bykov, V.J.N., Issaeva, N., Shilov, A., Hultcrantz, M., Pugacheva, E., Chumakov, P., Bergman, J., Wiman, K.G., and Selivanova, G. (2002). Restoration of the tumor suppressor function to mutant p53 by a low-molecular-weight compound. *Nat. Med.* 8, 282–288.

Cancer Genome Atlas Research Network. (2011). Integrated genomic analyses of ovarian carcinoma. *Nature* 474, 609–615.

Chen, C.L., Ip, S.M., Cheng, D., Wong, L.C., and Ngan, H.Y. (2000). P73 gene expression in ovarian cancer tissues and cell lines. *Clin. Cancer Res.* 6, 3910–3915.

Eisenberg, D., and Jucker, M. (2012). The amyloid state of proteins in human diseases. *Cell* 148, 1188–1203.

Freed-Pastor, W.A., Mizuno, H., Zhao, X., Langerød, A., Moon, S.-H., Rodriguez-Barrueco, R., Barsotti, A., Chicas, A., Li, W., Polotskaia, A., et al. (2012). Mutant p53 disrupts mammary tissue architecture via the mevalonate pathway. *Cell* 148, 244–258.

Fuchs, S.M., and Raines, R.T. (2005). Polyarginine as a multifunctional fusion tag. *Protein Sci.* 14, 1538–1544.

Ghosh, S., Ghosh, D., Ranganathan, S., Anoop, A., P, S.K., Jha, N.N., Padinhateeri, R., and Maji, S.K. (2014). Investigating the intrinsic aggregation potential of evolutionarily conserved segments in p53. *Biochemistry* 53, 5995–6010.

Goldschmidt, L., Teng, P.K., Riek, R., and Eisenberg, D. (2010). Identifying the amyloids, proteins capable of forming amyloid-like fibrils. *Proc. Natl. Acad. Sci. USA* 107, 3487–3492.

Härd, T., and Lendel, C. (2012). Inhibition of amyloid formation. *J. Mol. Biol.* 421, 441–465.

Hashimoto, K., Morishige, K., Sawada, K., Tahara, M., Kawagishi, R., Ikebuchi, Y., Sakata, M., Tasaka, K., and Murata, Y. (2005). Alendronate inhibits intraperitoneal dissemination in in vivo ovarian cancer model. *Cancer Res.* 65, 540–545.

Issaeva, N., Friedler, A., Bozko, P., Wiman, K.G., Fersht, A.R., and Selivanova, G. (2003). Rescue of mutants of the tumor suppressor p53 in cancer cells by a designed peptide. *Proc. Natl. Acad. Sci. USA* 100, 13303–13307.

Janzen, D.M., Tiourin, E., Salehi, J.A., Paik, D.Y., Lu, J., Pellegrini, M., and Memarzadeh, S. (2015). An apoptosis-enhancing drug overcomes platinum resistance in a tumour-initiating subpopulation of ovarian cancer. *Nat. Commun.* 6, 7956.

Joerger, A.C., and Fersht, A.R. (2008). Structural biology of the tumor suppressor p53. *Annu. Rev. Biochem.* 77, 557–582.

Khoo, K.H., Verma, C.S., and Lane, D.P. (2014). Drugging the p53 pathway: understanding the route to clinical efficacy. *Nat. Rev. Drug Discov.* 13, 217–236.

Knight, L.A., Kurbacher, C.M., Glaysher, S., Fernando, A., Reichelt, R., Dexel, S., Reinhold, U., and Cree, I.A. (2009). Activity of mevalonate pathway inhibitors against breast and ovarian cancers in the ATP-based tumour chemosensitivity assay. *BMC Cancer* 9, 38.

Kruiswijk, F., Labuschagne, C.F., and Vousden, K.H. (2015). p53 in survival, death and metabolic health: a lifeguard with a licence to kill. *Nat. Rev. Mol. Cell Biol.* 16, 393–405.

Kurman, R.J., and Shih, I.-M. (2008). Pathogenesis of ovarian cancer: lessons from morphology and molecular biology and their clinical implications. *Int. J. Gynecol. Pathol.* 27, 151–160.

Lane, D.P., and Crawford, L.V. (1979). T antigen is bound to a host protein in SY40-transformed cells. *Nature* 278, 261–263.

- Lasagna-Reeves, C.A., Clos, A.L., Castillo-Carranza, D., Sengupta, U., Guerrero-Muñoz, M., Kelly, B., Wagner, R., and Kayed, R. (2013). Dual role of p53 amyloid formation in cancer; loss of function and gain of toxicity. *Biochem. Biophys. Res. Commun.* 430, 963–968.
- Leaver-Fay, A., Tyka, M., Lewis, S.M., Lange, O.F., Thompson, J., Jacak, R., Kaufman, K., Renfrew, P.D., Smith, C.A., Sheffler, W., et al. (2011). ROSETTA3: an object-oriented software suite for the simulation and design of macromolecules. *Methods Enzymol.* 487, 545–574.
- Lehmann, S., Bykov, V.J.N., Ali, D., Andrén, O., Cherif, H., Tidefelt, U., Ugglä, B., Yachnin, J., Juliusson, G., Moshfegh, A., et al. (2012). Targeting p53 in vivo: a first-in-human study with p53-targeting compound APR-246 in refractory hematologic malignancies and prostate cancer. *J. Clin. Oncol.* 30, 3633–3639.
- Leitao, M.M., Soslow, R.A., Baergen, R.N., Olvera, N., Arroyo, C., and Boyd, J. (2004). Mutation and expression of the TP53 gene in early stage epithelial ovarian carcinoma. *Gynecol. Oncol.* 93, 301–306.
- L'Espérance, S., Bachvarova, M., Tetu, B., Mes-Masson, A.-M., and Bachvarov, D. (2008). Global gene expression analysis of early response to chemotherapy treatment in ovarian cancer spheroids. *BMC Genomics* 9, 99.
- Levine, A.J., and Oren, M. (2009). The first 30 years of p53: growing ever more complex. *Nat. Rev. Cancer* 9, 749–758.
- Levy, C.B., Stumbo, A.C., Ano Bom, A.P.D., Portari, E.A., Cordeiro, Y., Carneiro, Y., Silva, J.L., and De Moura-Gallo, C.V. (2011). Co-localization of mutant p53 and amyloid-like protein aggregates in breast tumors. *Int. J. Biochem. Cell Biol.* 43, 60–64.
- Linzer, D.I.H., and Levine, A.J. (1979). Characterization of a 54K Dalton cellular SV40 tumor antigen present in SV40-transformed cells and uninfected embryonal carcinoma cells. *Cell* 17, 749–758.
- Liu, X., Wilcken, R., Joerger, A.C., Chuckowree, I.S., Amin, J., Spencer, J., and Fersht, A.R. (2013). Small molecule induced reactivation of mutant p53 in cancer cells. *Nucleic Acids Res.* 41, 6034–6044.
- Martirosyan, A., Clendening, J.W., Goard, C.A., and Penn, L.Z. (2010). Lovastatin induces apoptosis of ovarian cancer cells and synergizes with doxorubicin: potential therapeutic relevance. *BMC Cancer* 10, 103.
- Morgan, R.J., Alvarez, R.D., Armstrong, D.K., Burger, R.A., Chen, L., Copeland, L., Crispens, M.A., Gershenson, D.M., Gray, H.J., Hakam, A., et al. (2013). Ovarian cancer, version 2.2013. *J. Natl. Compr. Canc Netw.* 11, 1199–1209.
- Muller, P.A.J., and Vousden, K.H. (2013). p53 mutations in cancer. *Nat. Cell Biol.* 15, 2–8.
- Naora, H., and Montell, D.J. (2005). Ovarian cancer metastasis: integrating insights from disparate model organisms. *Nat. Rev. Cancer* 5, 355–366.
- Petitjean, A., Mathe, E., Kato, S., Ishioka, C., Tavtigian, S.V., Hainaut, P., and Olivier, M. (2007). Impact of mutant p53 functional properties on TP53 mutation patterns and tumor phenotype: lessons from recent developments in the IARC TP53 database. *Hum. Mutat.* 28, 622–629.
- Rieber, M., and Strasberg-Rieber, M. (2012). Hypoxia, Mn-SOD and H₂O₂ regulate p53 reactivation and PRIMA-1 toxicity irrespective of p53 status in human breast cancer cells. *Biochem. Pharmacol.* 84, 1563–1570.
- Rufini, A., Agostini, M., Grespi, F., Tomasini, R., Sayan, B.S., Niklison-Chirou, M.V., Conforti, F., Velletri, T., Mastino, A., Mak, T.W., et al. (2011). p73 in cancer. *Genes Cancer* 2, 491–502.
- Sawaya, M.R., Sambashivan, S., Nelson, R., Ivanova, M.I., Sievers, S.A., Apostol, M.I., Thompson, M.J., Balbirnie, M., Wiltzius, J.J.W., McFarlane, H.T., et al. (2007). Atomic structures of amyloid cross-beta spines reveal varied steric zippers. *Nature* 447, 453–457.
- Seidman, J.D., Horkayne-Szakaly, I., Haiba, M., Boice, C.R., Kurman, R.J., and Ronnett, B.M. (2004). The histologic type and stage distribution of ovarian carcinomas of surface epithelial origin. *Int. J. Gynecol. Pathol.* 23, 41–44.
- Siddik, Z.H. (2003). Cisplatin: mode of cytotoxic action and molecular basis of resistance. *Oncogene* 22, 7265–7279.
- Siegel, R., Ma, J., Zou, Z., and Jemal, A. (2014). Cancer statistics, 2014. *CA Cancer J. Clin.* 64, 9–29.
- Sievers, S.A., Karanickolas, J., Chang, H.W., Zhao, A., Jiang, L., Zirafi, O., Stevens, J.T., Münch, J., Baker, D., and Eisenberg, D. (2011). Structure-based design of non-natural amino-acid inhibitors of amyloid fibril formation. *Nature* 475, 96–100.
- Silva, J.L., Gallo, C.V.D.M., Costa, D.C.F., and Rangel, L.P. (2014). Prion-like aggregation of mutant p53 in cancer. *Trends Biochem. Sci.* 39, 260–267.
- Tophkhane, C., Yang, S.-H., Jiang, Y., Ma, Z., Subramaniam, D., Anant, S., Yogosawa, S., Sakai, T., Liu, W.-G., Edgerton, S., et al. (2012). p53 inactivation upregulates p73 expression through E2F-1 mediated transcription. *PLoS One* 7, e43564.
- Vassilev, L.T., Vu, B.T., Graves, B., Carvajal, D., Podlaski, F., Filipovic, Z., Kong, N., Kammlott, U., Lukacs, C., Klein, C., et al. (2004). In vivo activation of the p53 pathway by small-molecule antagonists of MDM2. *Science* 303, 844–848.
- Vaughan, S., Coward, J.I., Bast, R.C., Berchuck, A., Berek, J.S., Brenton, J.D., Coukos, G., Crum, C.C., Drapkin, R., Etemadmoghadam, D., et al. (2011). Rethinking ovarian cancer: recommendations for improving outcomes. *Nat. Rev. Cancer* 11, 719–725.
- Vaughan, C.A., Frum, R., Pearsall, I., Singh, S., Windle, B., Yeudall, A., Deb, S.P., and Deb, S. (2012). Allele specific gain-of-function activity of p53 mutants in lung cancer cells. *Biochem. Biophys. Res. Commun.* 428, 6–10.
- Vazquez, A., Bond, E.E., Levine, A.J., and Bond, G.L. (2008). The genetics of the p53 pathway, apoptosis and cancer therapy. *Nat. Rev. Drug Discov.* 7, 979–987.
- Ventura, A., Kirsch, D.G., McLaughlin, M.E., Tuveson, D.A., Grimm, J., Lintault, L., Newman, J., Reczek, E.E., Weissleder, R., and Jacks, T. (2007). Restoration of p53 function leads to tumour regression in vivo. *Nature* 445, 661–665.
- Vossio, S., Palescandolo, E., Pediconi, N., Moretti, F., Balsano, C., Levrero, M., and Costanzo, A. (2002). DN-p73 is activated after DNA damage in a p53-dependent manner to regulate p53-induced cell cycle arrest. *Oncogene* 21, 3796–3803.
- Vousden, K.H., and Ryan, K.M. (2009). p53 and metabolism. *Nat. Rev. Cancer* 9, 691–700.
- Wang, G., and Fersht, A.R. (2012). First-order rate-determining aggregation mechanism of p53 and its implications. *Proc. Natl. Acad. Sci. USA* 109, 13590–13595.
- Wilcken, R., Wang, G., Boeckler, F.M., and Fersht, A.R. (2012). Kinetic mechanism of p53 oncogenic mutant aggregation and its inhibition. *Proc. Natl. Acad. Sci. USA* 109, 13584–13589.
- Xu, J., Reumers, J., Couceiro, J.R., De Smet, F., Gallardo, R., Rudyak, S., Cornelis, A., Rozenski, J., Zwolinska, A., Marine, J.-C., et al. (2011). Gain of function of mutant p53 by coaggregation with multiple tumor suppressors. *Nat. Chem. Biol.* 7, 285–295.
- Yu, X., Vazquez, A., Levine, A.J., and Carpizo, D.R. (2012). Allele specific p53 mutant reactivation. *Cancer Cell* 21, 614–625.

Supplemental Information

A Designed Inhibitor of p53 Aggregation Rescues

p53 Tumor Suppression in Ovarian Carcinomas

Alice Soragni, Deanna M. Janzen, Lisa M. Johnson, Anne G. Lindgren, Anh Thai-Quynh Nguyen, Ekaterina Tiourin, Angela B. Soriaga, Jing Lu, Lin Jiang, Kym F. Faull, Matteo Pellegrini, Sanaz Memarzadeh, and David S. Eisenberg

SUPPLEMENTAL INFORMATION

A designed inhibitor of p53 aggregation rescues p53 tumor-suppression in ovarian carcinomas

Alice Soragni, Deanna M. Janzen, Lisa M. Johnson, Anne G. Lindgren, Anh Thai-Quynh Nguyen, Ekaterina Tiourin, Angela B. Soriaga, Jing Lu, Lin Jiang, Kym F. Faull, Matteo Pellegrini, Sanaz Memarzadeh and David S. Eisenberg

SUPPLEMENTAL DATA

Table S1 (refers to Figure 1). Statistics of X-ray data collection and atomic refinement of fibril-like crystal structures of two p53 segments. **a.** Values in parentheses correspond to the highest resolution shell. **b.** $R_{\text{merge}} = \sum |I - \langle I \rangle| / \sum I$. **c.** $R_{\text{work}} = \sum |F_o - F_c| / \sum F_o$. **d.** $R_{\text{free}} = \sum |F_o - F_c| / \sum F_o$, calculated using a random set containing 10% of reflections that were not included throughout structure refinement.

Crystal parameters		
Segment sequence	252-LTIITLE-258	253-TIITLE-258
PDB code	4RP6	4RP7
Space group	P1	C2
Cell dimensions:		
a, b, c (Å)	4.81, 12.60, 21.34	43.02, 4.85, 19.77
α, β, γ (°)	86.59, 89.29, 79.15	90, 92.12, 90
Molecules in Asymmetric Unit	1	1
Data collection		
Synchrotron beamline	APS (24-ID-E)	APS (24-ID-E)
Wavelength (Å)	0.9792	0.9792
Resolution range (Å)	1.70	1.58
Unique Reflections	507	635
Overall Redundancy	3.1 (2.6) ^a	4.0 (3.0)
Completeness (%)	97.0 (91.4)	96.5 (87.7)
R_{merge} (%) ^b	9.6 (50.5)	11.4 (32.9)
$\langle I/\sigma I \rangle$	10.6 (2.9)	8.9 (4.1)
Refinement		
Resolution (Å)	21.30-1.70	21.49 – 1.58
R_{work} (%) ^c	16.2	16.4
R_{free} (%) ^d	19.2	19.3
No. atoms:		
Protein	59	48
Ligand/ion	0	1
Water	2	2
Overall B-factors	12.7	3.1
R.m.s. deviation:		
Bond length (Å)	0.007	0.009
Bond angle (°)	1.080	1.861

Table S2 (Refers to Figure 1). Computed aggregation propensities and capping energies of eight designed p53 aggregation-targeting peptides. **a.** Predicted full-atom energy of interactions across the zipper interface formed by possible self-association for each capping peptide inhibitor. Those with significant aggregating propensities are in red and were discarded for this reason from further analysis. **b.** Predicted full-atom energy of interactions across the binding interface between the capping peptide inhibitor and the LTIITLE fibril core. Notice that LTRITLE has the lowest aggregation propensity and was selected as a promising candidate for rescuing activity of aggregating p53.

	Zipper energy ^a (kcal/mol)	Capping energy ^b			
		Single Sheet		Triple Sheet	
		absolute (kcal/mol)	relative to LTIITLE	absolute (kcal/mol)	relative to LTIITLE
LTIITLE (native)	-26.2	-42.2	0.0	-86.2	0.0
LTRITLE	-18.2	-40.5	1.7	-84.6	1.6
LTRIYLE	-19.5	-41.0	1.1	-85.2	1.0
YTRITLE	-19.3	-40.3	1.9	-83.5	2.6
YTRIYLE	-19.8	-41.3	0.8	-85.3	0.9
ETRITLE	-19.0	-39.8	2.4	-83.0	3.1
LTKITLE	-25.5	-41.2	0.9	-84.0	2.2
WTKITLE	-24.3	-40.1	2.1	-82.1	4.0
YTKITLE	-24.1	-40.8	1.3	-82.5	3.6

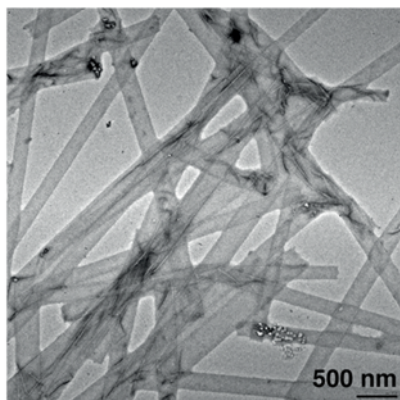
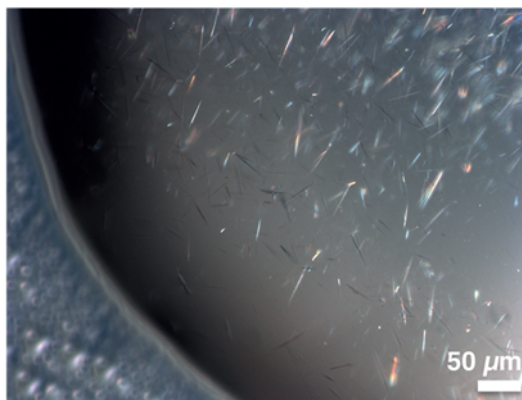
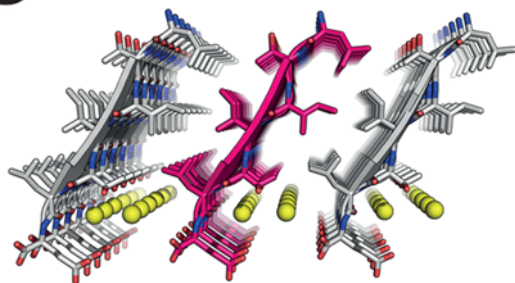
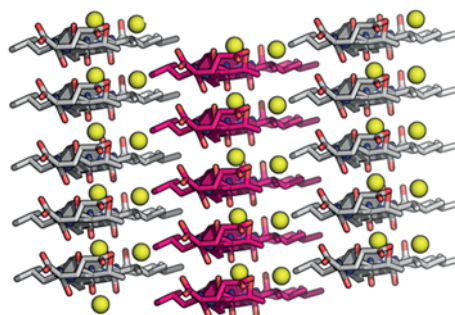
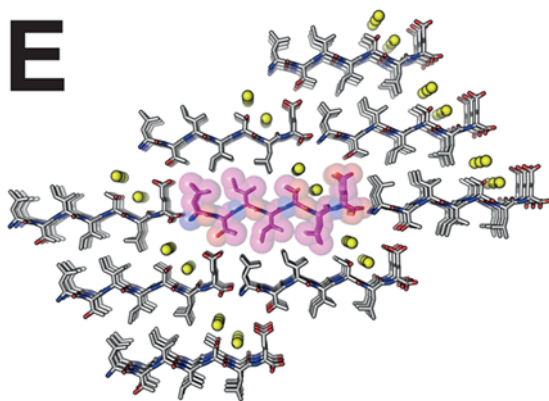
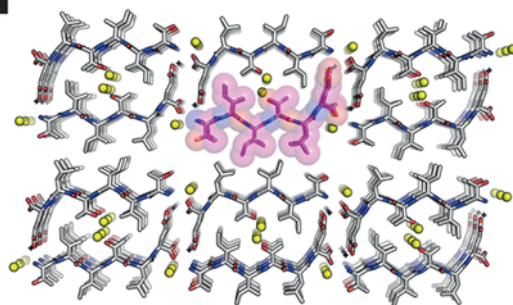
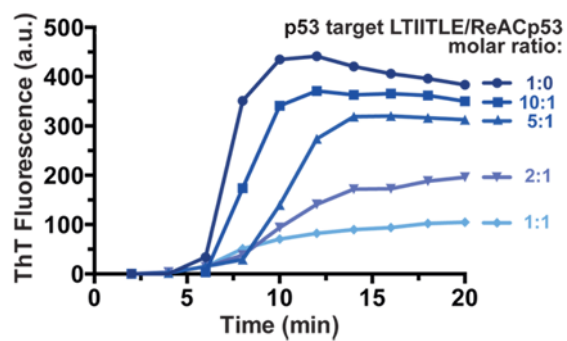
A**B****C****D****E****F****G**

Figure S1. Structures of p53 amyloid spines at atomic resolution and inhibition of LTIITLE aggregation by ReACp53 (Refers to Fig. 1). **A.** The p53 segment LTIITLE forms amyloid-like fibrils in solution. **B.** The same segment formed microcrystals. **C.** Structure of the Class 2 steric zipper formed by residues 252-258 (sequence LTIITLE), viewed down the fibril axis. Water molecules are depicted as yellow spheres. **D.** Side view of the same structure perpendicular to the fibril axis highlights the tight side-chain interdigitation which stabilizes the fibril spine. **E.** and **F.** Crystal contacts for the p53₂₅₂₋₂₅₈ (sequence LTIITLE) and p53₂₅₃₋₂₅₈ (sequence TIITLE) structures. The atoms in the center (red) unit cell are shown as spheres representing van der Waals radii. **G.** Aggregation of the p53 target segment is monitored by the Thioflavin T assay. An increase in Thioflavin T fluorescence is detected over time due to the formation of increasing amounts of amyloids to which the dye can bind. ReACp53 is added in solution at five different concentrations and delays the aggregation onset and lowers the total amount of aggregates present, in a concentration dependent fashion.

Table S3 (Refers to Figures 2, 4 and 5). List of clinical samples used in this study. h: heterozygous; *: stop codon.

Name	Age	Diagnosis	Stage	Previous treatment	Origin	p53 status	ReACp53 sensitivity
Patient 1	73	HGSOC	IIIB	None	Primary tumor	P72R/R248Q	+++
Patient 2	50	HGSOC	IIIC	None	Primary tumor	P72R/R196*h/R248Q	+++
Patient 3	80	HGSOC	IIIC	Carboplatin and Taxol	Primary tumor	R248Q	+++
Patient 4	70	HGSOC	IIIC	None	Primary tumor	P72R/I125S	+++
Patient 5	74	HGSOC	IIIC	None	Primary tumor	V272M	+
Patient 6	42	HGSOC	IIIC	None	Primary tumor	P72R/Y234C	+++
Patient 7	65	HGSOC	IV	None	Primary tumor	P72R/Y326L	+++
Ctr Patient 8	65	Endometrioid OC	I	None	Primary tumor	P72R	-

Table S4 (Refers to Figures 2 - 7). p53 status of the cell lines used in this study

Name	Origin	p53 status
OVCAR3	HGSOC	R248Q
MCF 7	Breast Cancer	WT
SKOV3	Ovarian carcinoma	H179R (null)
Detroit 562	Head and Neck	R175H
S1 GODL	Stable cell line derived from Patient 1	P72R/R248Q

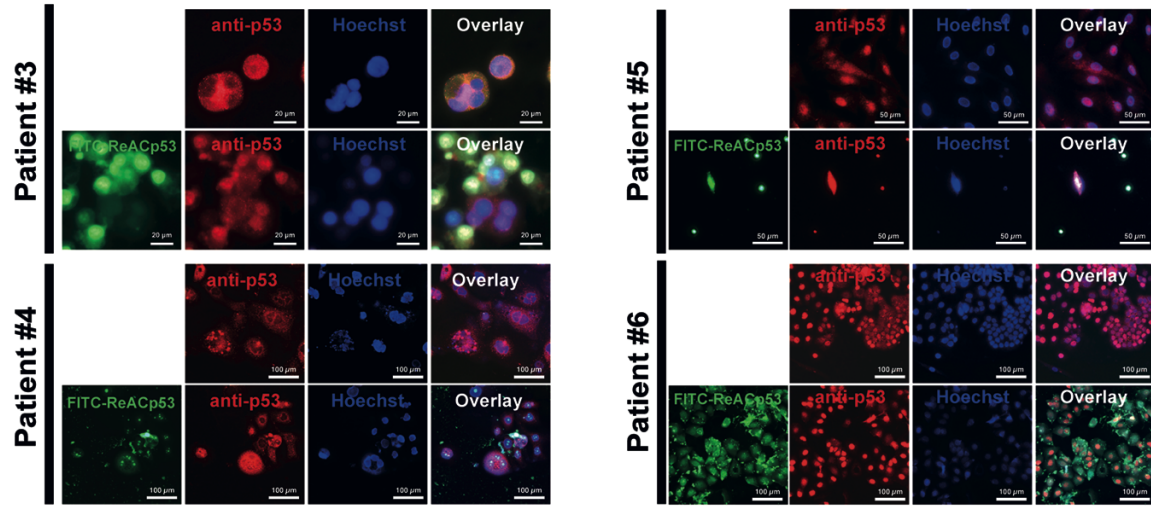
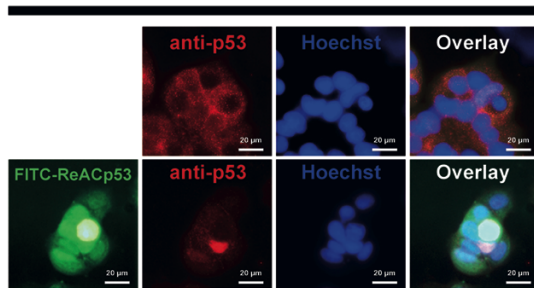
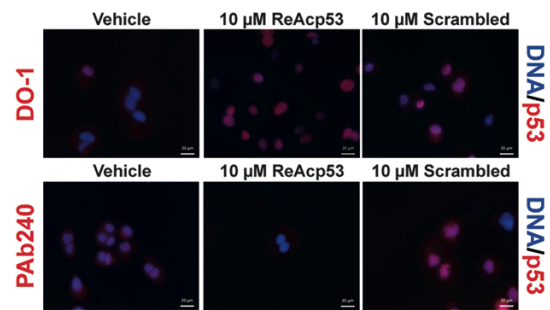
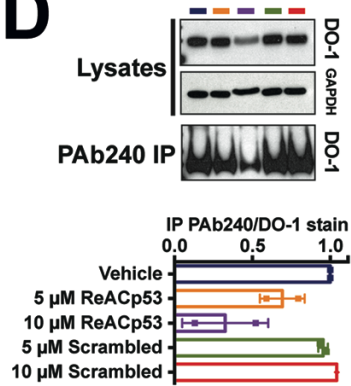
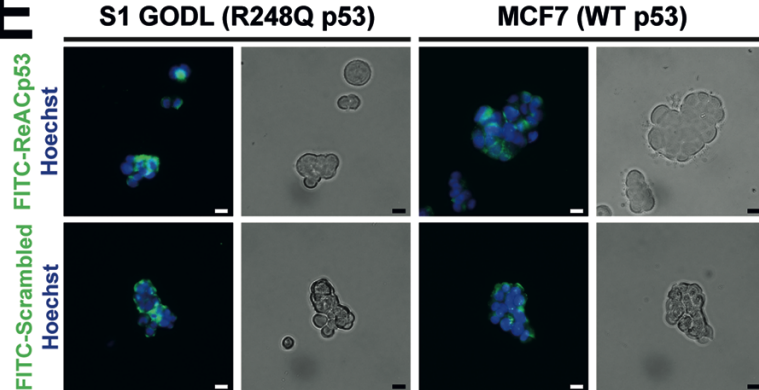
A**B****MCF7 (p53 WT)****C****S1 GODL (p53 R248Q)****D****E**

Figure S2 (Refers to Figure 2). ReACp53 inhibits p53 aggregation and re-localizes p53 to the nucleus in primary cells from HGSOC patients containing mutant p53. A. Additional HGSOC patient samples containing mutant p53 mostly localized to the cytosol prior to treatment. After a 20h exposure to 10 μ M ReACp53, p53 is now diffuse and mostly nuclear. A FITC-labeled ReACp53 is used in this experiment to follow cell penetration and localization of the peptide. **B.** The localization of p53 in control cells bearing WT p53 (MCF7) does not change upon ReACp53 treatment. **C.** Control experiment showing that the effects on p53 folding and localization observed in S1 GODL cells are brought about by ReACp53 but not a scrambled peptide control. **D.** Partially unfolded/aggregated p53 immunoprecipitated with PAb240 from S1 GODL native lysates. The quantification includes two independent experiments as symbols and the average as bars. For input and IP blots, samples are color-coded as in the quantification (blue: vehicle, yellow: 5 μ M ReACp53, purple: 10 μ M ReACp53, green: 5 μ M Scrambled, red: 10 μ M Scrambled). Symbols represent independent IP experiments, bars are average \pm SD. **E.** FITC-labeled ReACp53 or scrambled peptide penetrates organoids in culture. Scale bars: 20 μ m.

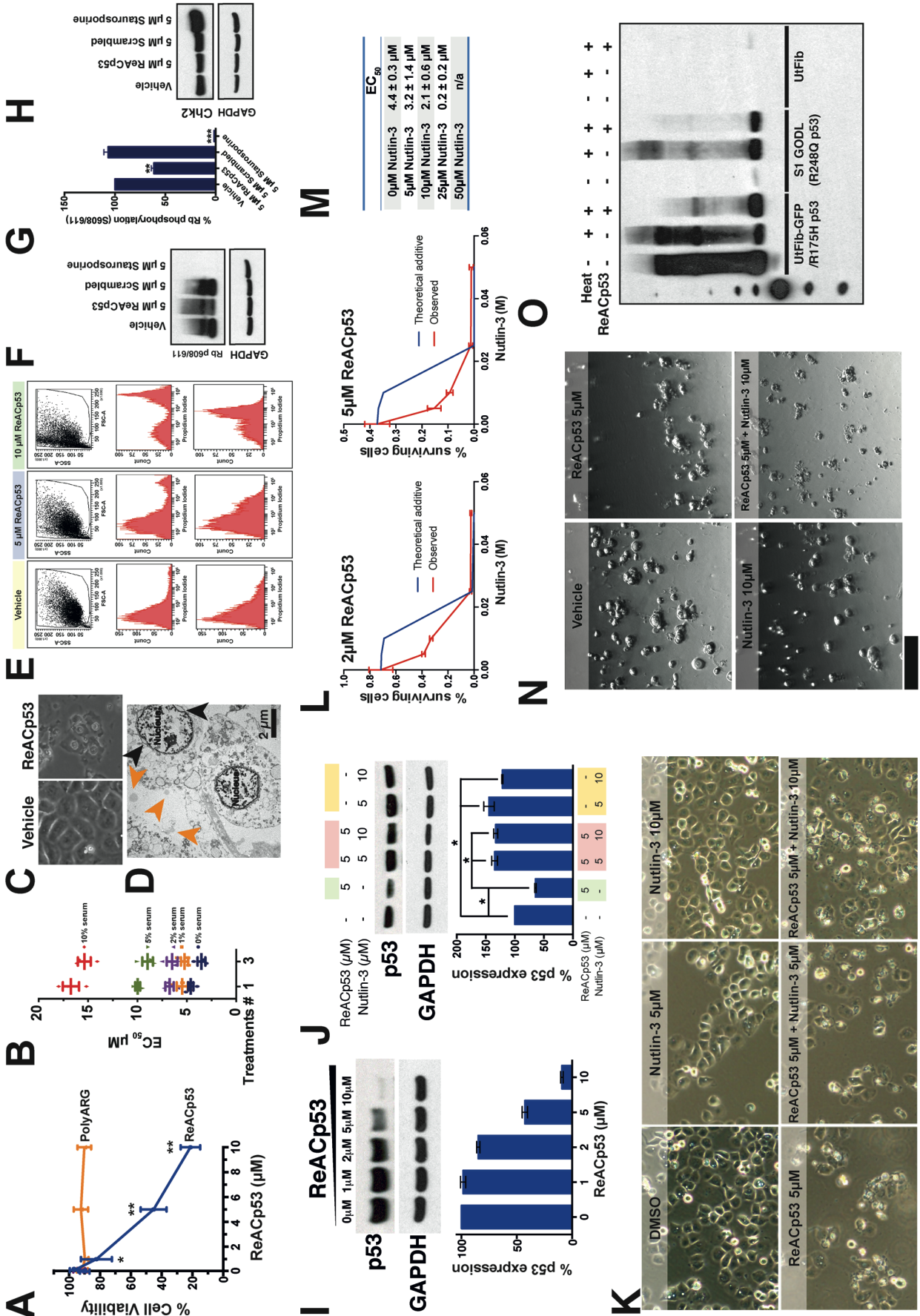
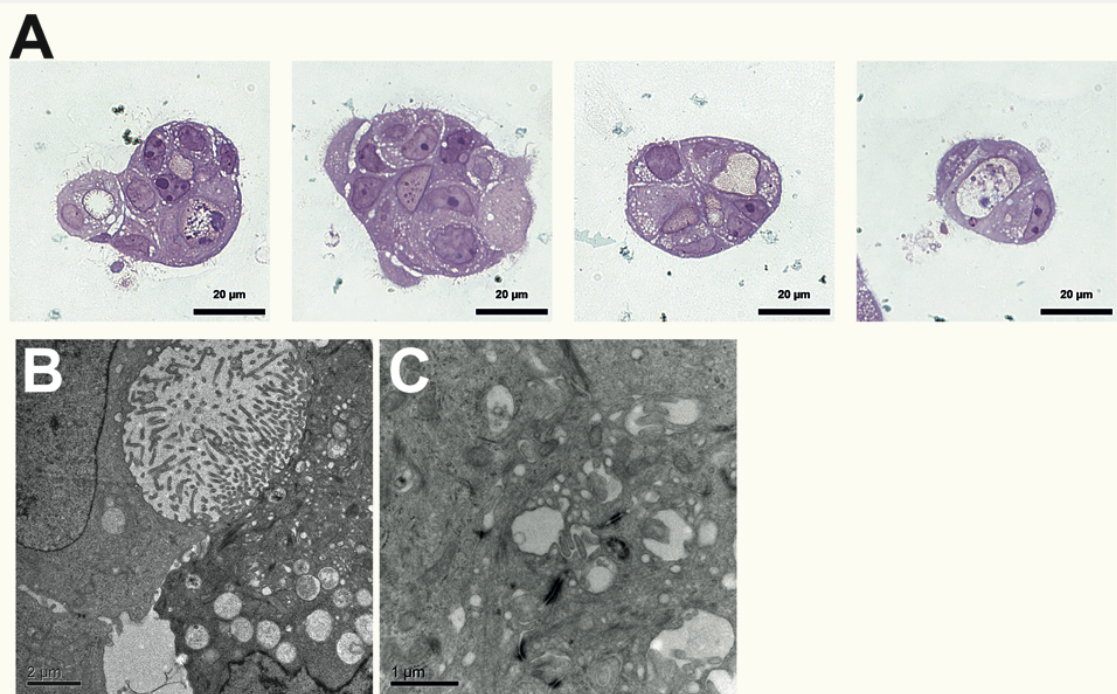
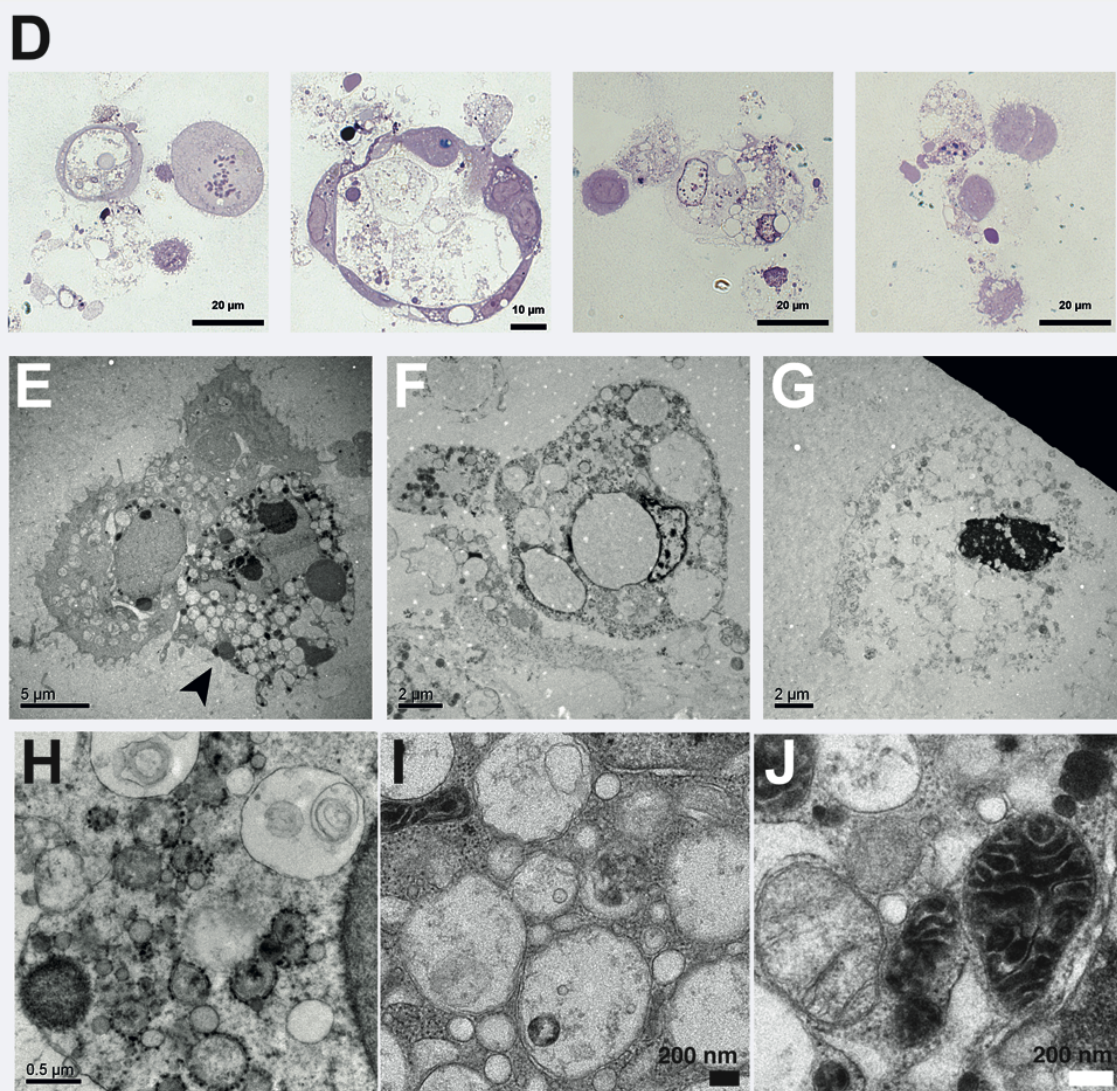


Figure S3 (Refers to Figures 3). ReACp53 causes cell death and cell cycle arrest and results in a concentration-dependent decrease of p53 levels in S1 GODL cells. **A.** A poly-arginine tag alone has no effect on cell viability of S1 GODL cells as measured by MTS assay. Symbols represent the average of three replicates; bars are SD. **B.** Multiple treatments reduce apparent EC_{50} values even in the presence of serum. Reference EC_{50} values calculated from three independent experiment ($n=3$) are shown as symbols, average \pm SEM as bars. **C.** The change in morphology in S1 GODL cells upon 16h of ReACp53 treatment as visualized by bright field microscopy. **D.** TEM image of S1 GODL cells treated with ReACp53. Signs of late apoptotic/necrotic cell death, such as condensed chromatin, an intact but enlarged nuclear envelope (black arrowheads) and isolated apoptotic bodies (orange arrowheads) are visible. **E.** Forward- and Side- scatter plots and histograms for a representative example of S1 GODL cells stained with YO-PRO-1/PI quantified in Figure 3D. **F.** S1 GODL cells treated for 4-5 hours with ReACp53 exhibited a marked decrease in Phospho-Rb (Ser807/811), quantified in **G.** and compatible with a G0/G1 cell cycle arrest. **H.** ReACp53 treatment of S1 GODL cells for 4-5 hours did not result in DNA damage, as seen by no induction of phospho-Chk2. High concentration of Staurosporine in the control sample induced hyperphosphorylation of Chk2, as Staurosporine has been reported to damage DNA in those concentration ranges. **I.** Concentration-dependent decrease in p53 levels upon 16h of ReACp53 treatment of S1 GODL cells as assessed by Western Blot. p53 was detected by DO-1 antibody. One representative experiment shown ($n=3$). **J.** Addition of Nutlin-3, a p53-MDM2 interaction inhibitor, increases p53 levels in naive and ReACp53-treated samples. Quantification is normalized to GAPDH protein levels. GAPDH stain was performed on the same membrane after stripping. One representative experiment shown ($n=2$). $*p<0.05$. **K.** Despite having higher levels of mutant p53, cells treated with Nutlin-3 alone do not show cell changes compatible with cell death as visualized by light microscopy. **L. and M.** Nutlin-3 and ReACp53 synergize and reduce ReACp53 EC_{50} values. Cell viability is measured by MTS assay; all samples are measured in triplicates and reported as average \pm SD. One representative experiment is shown ($n=2$). **N.** Bright field image of S1 GODL organoids (100'000 cells/well) treated for 2 days with the indicated molecules. **O.** Western blot showing SDS-resistant p53 aggregates formed by heating native cell lysates to 42°C for 10 minutes stained with DO-1. Uterine fibroblasts infected with the GFP/R175H p53 construct have big amounts of immunoprecipitated p53 aggregates at baseline conditions. Heating the aggregates results in a high proportion of big SDS-resistant species that cannot enter the gel. Addition of 20 μ M ReACp53 to the lysates prior boiling results in a marked reduction of immunoprecipitated SDS-insoluble species when compared to the samples heated without ReACp53. Similar results are obtained with the R248Q p53 mutant in S1 GODL cells. Untransfected uterine fibroblasts were used as negative controls.

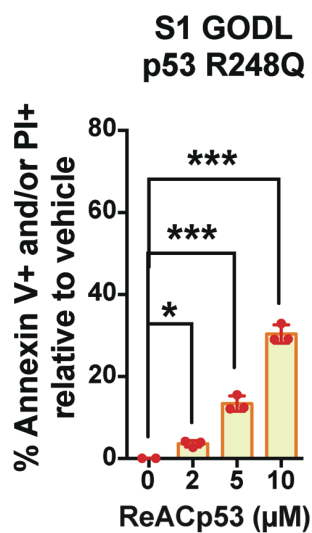
Vehicle



ReACp53

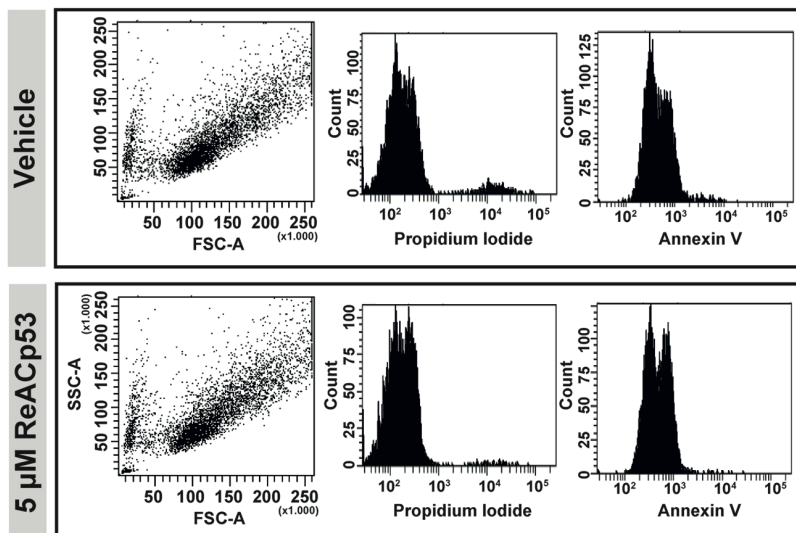


K



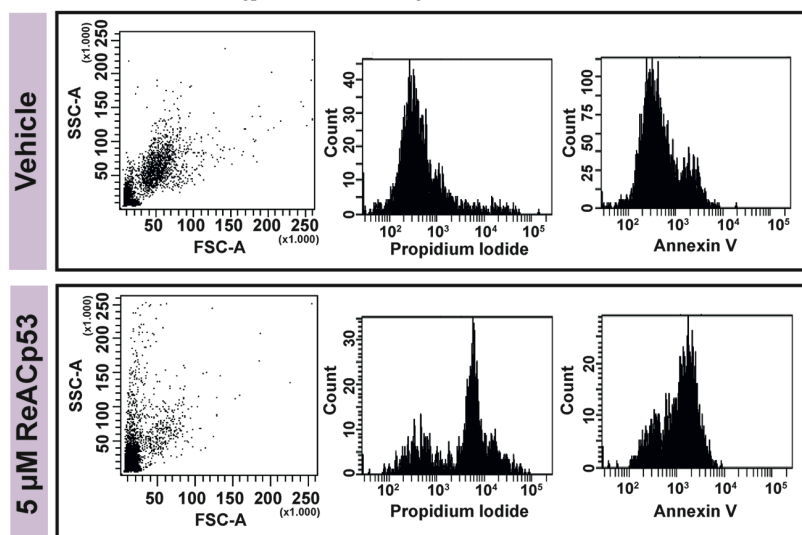
L

Patient #8 (p53 WT)



M

Patient #4 (p53 I251S)



N

Sample #ID	p53	EC ₅₀
MCF7	WT	N/A
Detroit562	R175H	2.3 μM
S1 GODL	R248Q	4.0 μM
Patient 1	P72R/R248Q	1.8 μM
Patient 2	P72R/R196*/R248Q	3.6 μM
Patient 3	R248Q	2.3 μM
Patient 5	V272M	6.7 μM
Patient 6	P72R/Y234C	3.5 μM
Patient 7	P72R/Y326L	6.6 μM
Patient 8	P72R	N/A

O

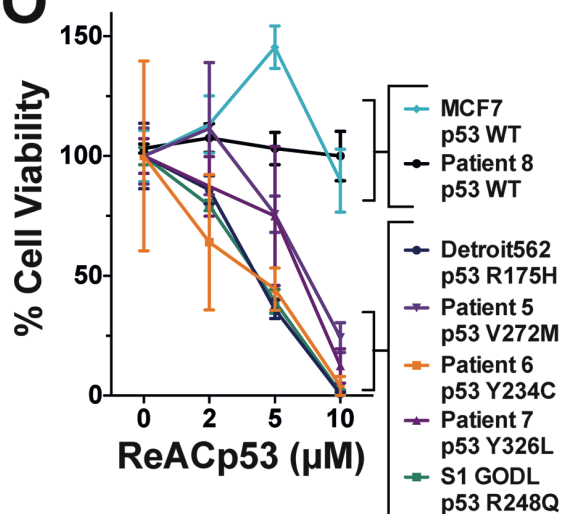
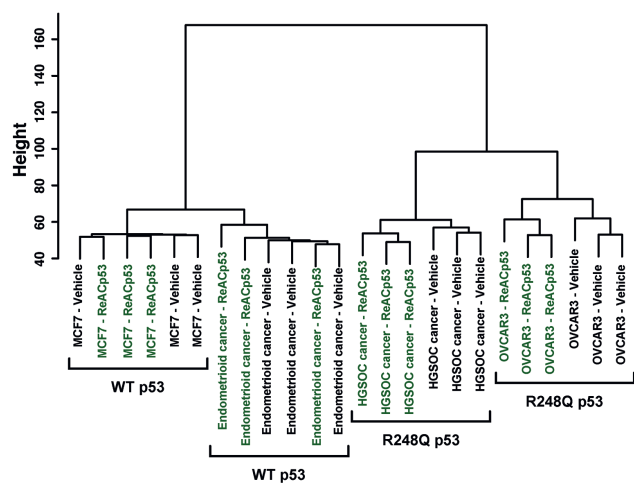
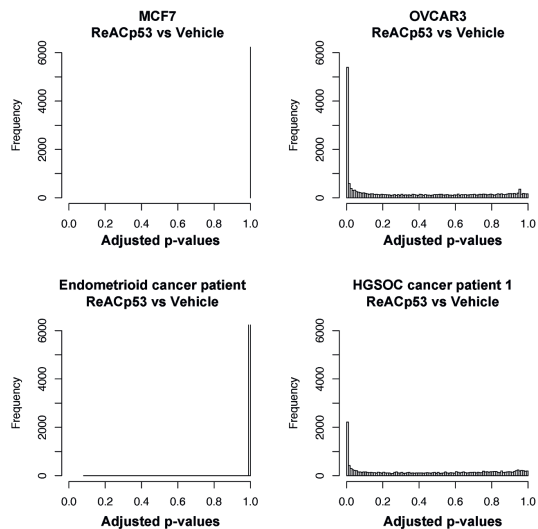


Figure S4 (Refers to Figure 4). Effects of ReACp53 on morphology and viability of organoids. **A.** Toluidine blue staining of semi-thin sections of organoids shows the internal architecture. Several cells constitute the sphere, with a number of internal cavities. **B.** A detail of the cavity is shown as visualized by TEM: several pili and small vesicles fill the hole. **C.** The cells in the organoid are closely packed, and tight junctions are visible by TEM at the cell-cell interface. **D.** Organoids treated with ReACp53 show complete disruption of their architecture. **E.** Some cells exhibit features of apoptotic cell death (arrowhead). **F. and G.** Other cells demonstrate more obvious necroptotic morphology with cell membrane disruption. **H.** At high magnification the enlarged ER is visible in the dying cells, as well as multiple multivesicular bodies. **I.** Several vesicles are visible in the cytosol of treated cells, as well as free ribosomes. **J.** Very condensed mitochondria are another feature of the treated cells. **K.** Annexin V/PI staining of S1 GODL cells upon two days of ReACp53 administration. Data presentation and statistic analysis as in Fig. 4E. **L. and M.** Representative examples of response to a 2-day ReACp53 treatment of organoids generated from primary cells derived from a control patient (#8, WT p53) and from the sensitive patient #4 (I251S p53). Forward- and Side- scatter plots and histograms for one biological replicate as quantified in Figure 4E. **N.** List of apparent EC₅₀ values for the clinical samples used in this study as determined from cell viability data obtained at day 7 (see Figure 4A for details on experiment design). **O.** Cell viability determined after a week of daily ReACp53 treatments by cell counting of triplicate samples.

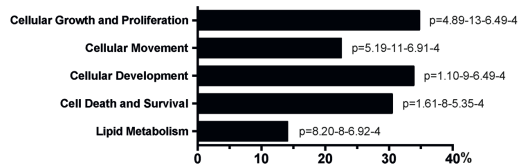
A



B



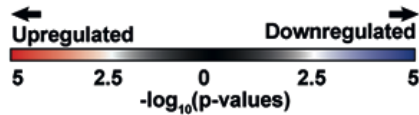
C



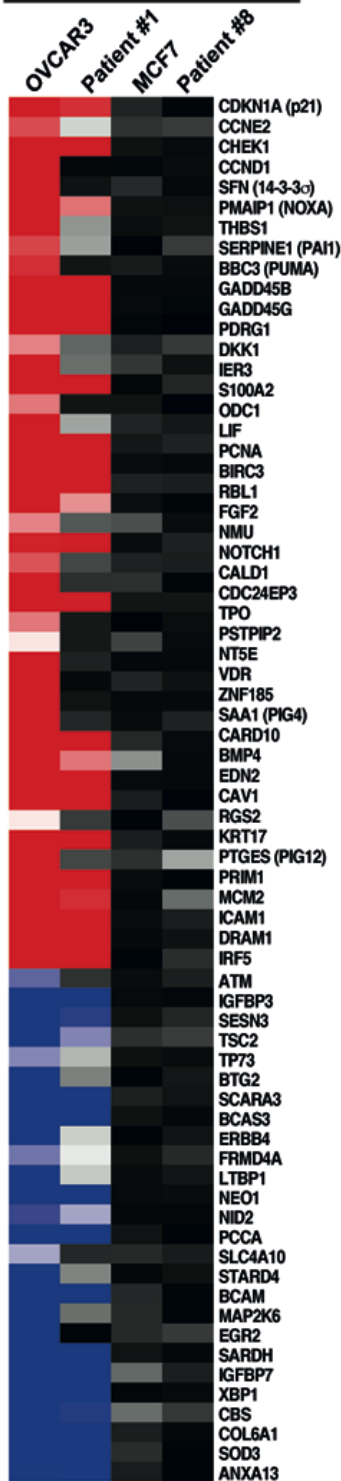
D

GO Terms	no. genes	p-value
oxidation reduction	63	1.70E-10
response to organic substance	79	8.40E-07
ion transport	71	7.00E-04
cell adhesion	65	1.10E-03
homeostatic process	59	4.80E-02
response to endogenous stimulus	55	7.40E-08
behavior	53	3.10E-05
cell-cell signaling	47	7.80E-02
neuron differentiation	44	1.90E-03
response to wounding	44	4.20E-02
lipid biosynthetic process	40	4.90E-05
cellular component morphogenesis	40	3.00E-03
generation of precursor metabolites and energy	37	2.50E-04
regulation of system process	36	4.10E-04
regulation of transcription	99	8.90E-04
regulation of RNA metabolic process	73	1.30E-03
regulation of cell proliferation	61	1.00E-12
regulation of cell death	54	8.00E-09
intracellular signaling cascade	49	1.70E-02
positive regulation of macromolecule metabolic process	48	7.70E-06
cell cycle	44	1.50E-05
response to wounding	42	3.70E-09
cell motion	39	5.90E-09
positive regulation of nitrogen compound metabolic process	39	1.20E-05
response to organic substance	39	1.40E-04
regulation of phosphate metabolic process	36	3.10E-07
positive regulation of molecular function	36	2.10E-05
defense response	36	5.70E-05

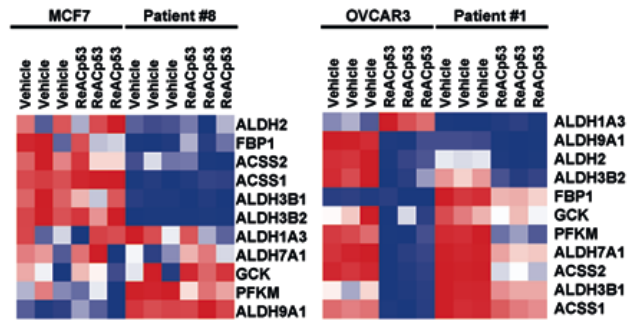
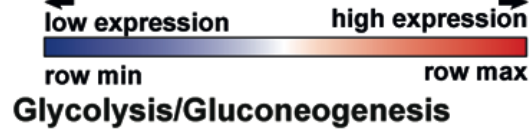
E



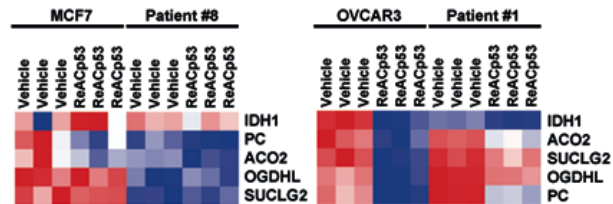
ReACp53 vs. vehicle



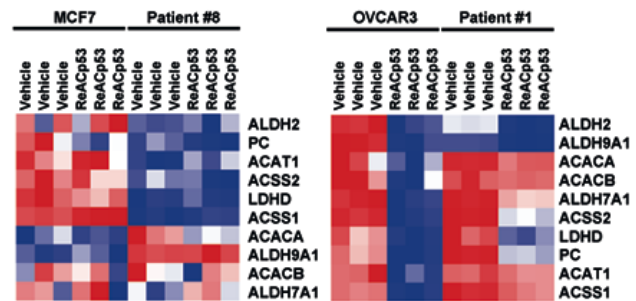
F



Citrate Cycle (TCA cycle)



Pyruvate Metabolism



Mevalonate Pathway

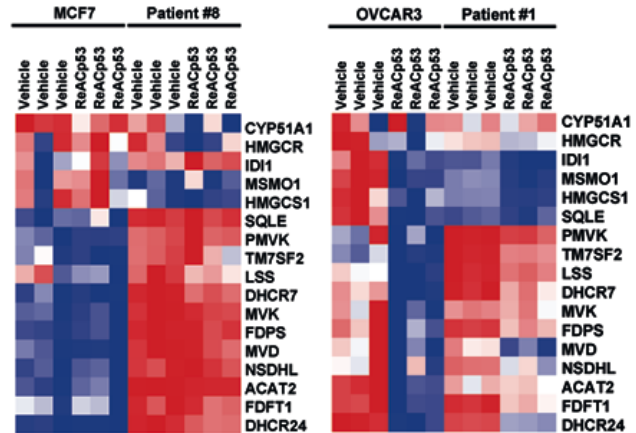


Figure S5 (Refers to Figure 5). **A.** Hierarchical clustering of results highlight how treated samples cluster together only in responsive cells. **B.** Adjusted p-value distribution for control and responsive samples. **C.** IPA analysis of molecular functions and processes for the HGSOC Patient 1 organoids. **D.** Gene Ontology analysis of the OVCAR3 results. The most highly represented terms for downregulated (blue box) and upregulated (red box) processes are listed. Redundant terms were removed. **E.** p-values for p53 pathway genes for the different samples (ReACp53 vs vehicle). Up-regulated genes are in red, downregulated in blue. **F.** Several metabolic pathways were downregulated in the treated samples. Components of pathways were assigned according to KEGG ontologies. Values are normalized within rows.

Table S5 (Refers to Figure 5). IPA upstream regulator analysis performed on OVCAR3 cells treated with 5 μ M ReAcP53 for 2 days reveals p53 as the most significant transcriptional regulator. The analysis was limited to transcription factors.

© 2000-2014 QIAGEN. All rights reserved.

Upstream Regulator	Molecule Type	p-value of overlap	Mechanistic Network
TP53	transcription regulator	6.10E-33	691 (20)
NFKBIA	transcription regulator	3.39E-20	548 (15)
JUN	transcription regulator	3.42E-17	715 (21)
RELA	transcription regulator	3.56E-17	598 (14)
CTNNB1	transcription regulator	2.09E-15	613 (22)
CEBPA	transcription regulator	3.47E-15	648 (25)
EPAS1	transcription regulator	2.10E-14	563 (19)
PDX1	transcription regulator	3.52E-14	615 (20)
CCND1	transcription regulator	1.22E-13	358 (13)
SP1	transcription regulator	1.28E-13	591 (24)
FOS	transcription regulator	3.79E-13	552 (17)
NOTCH1	transcription regulator	9.25E-13	477 (21)
MEOX2	transcription regulator	3.08E-12	530 (17)
HOXA10	transcription regulator	3.67E-12	233 (7)
HIF1A	transcription regulator	5.12E-12	627 (24)
CDKN2A	transcription regulator	2.59E-11	571 (22)
RB1	transcription regulator	4.02E-11	465 (15)
ZNF217	transcription regulator	4.04E-11	31 (2)
MYC	transcription regulator	6.44E-11	662 (18)
CEBPB	transcription regulator	6.99E-11	750 (22)
CREB1	transcription regulator	8.12E-11	596 (22)
SREBF2	transcription regulator	5.52E-10	424 (17)
PAX3	transcription regulator	5.80E-10	416 (7)
TP63	transcription regulator	6.27E-10	545 (22)
SMAD4	transcription regulator	8.18E-10	622 (21)
EHF	transcription regulator	1.74E-09	182 (7)
E2F1	transcription regulator	2.36E-09	435 (14)
SMARCA4	transcription regulator	2.58E-09	602 (21)
NKX2-1	transcription regulator	4.57E-09	259 (7)
HDAC1	transcription regulator	5.12E-09	593 (21)
NEUROG1	transcription regulator	5.16E-09	
HTT	transcription regulator	5.28E-09	718 (22)
EZH2	transcription regulator	6.07E-09	616 (24)
TWIST1	transcription regulator	7.07E-09	589 (22)
NFKB1	transcription regulator	1.00E-08	543 (12)
FOXO1	transcription regulator	1.57E-08	609 (21)
STAT3	transcription regulator	4.65E-08	633 (15)
RBPJ	transcription regulator	5.03E-08	553 (22)
SMARCB1	transcription regulator	5.05E-08	562 (19)
DACH1	transcription regulator	5.82E-08	488 (12)
SP3	transcription regulator	5.88E-08	530 (19)
SRF	transcription regulator	8.90E-08	418 (18)
TP73	transcription regulator	9.58E-08	571 (21)
EP300	transcription regulator	1.37E-07	685 (21)
GLI1	transcription regulator	1.38E-07	638 (24)
SREBF1	transcription regulator	1.70E-07	494 (18)
NKX2-3	transcription regulator	1.70E-07	
BRCA1	transcription regulator	1.72E-07	578 (21)
KLF2	transcription regulator	2.04E-07	522 (17)
SMAD1	transcription regulator	2.07E-07	548 (19)
FOSL1	transcription regulator	2.54E-07	295 (9)
HIC1	transcription regulator	2.54E-07	359 (11)
E2F3	transcription regulator	3.53E-07	548 (21)
KLF5	transcription regulator	3.63E-07	570 (20)
KLF4	transcription regulator	6.91E-07	596 (21)
RUNX1	transcription regulator	6.98E-07	727 (18)
EGR1	transcription regulator	7.01E-07	695 (17)
SOX2	transcription regulator	7.18E-07	61 (4)
MITF	transcription regulator	8.60E-07	
FOXO4	transcription regulator	9.07E-07	527 (18)
WT1	transcription regulator	9.33E-07	580 (18)
SMAD3	transcription regulator	1.26E-06	676 (21)
GFI1	transcription regulator	1.45E-06	424 (11)
SPDEF	transcription regulator	2.08E-06	525 (11)
HMGA1	transcription regulator	2.36E-06	605 (21)
SIAH2	transcription regulator	2.92E-06	512 (13)
NCOR1	transcription regulator	3.06E-06	603 (21)
TFEB	transcription regulator	3.18E-06	
POU2F1	transcription regulator	3.23E-06	537 (11)
TCF12	transcription regulator	6.04E-06	
FOXA2	transcription regulator	7.74E-06	450 (17)
FOXO3	transcription regulator	7.74E-06	668 (25)
SMAD7	transcription regulator	8.43E-06	546 (20)
E2F2	transcription regulator	9.55E-06	174 (10)

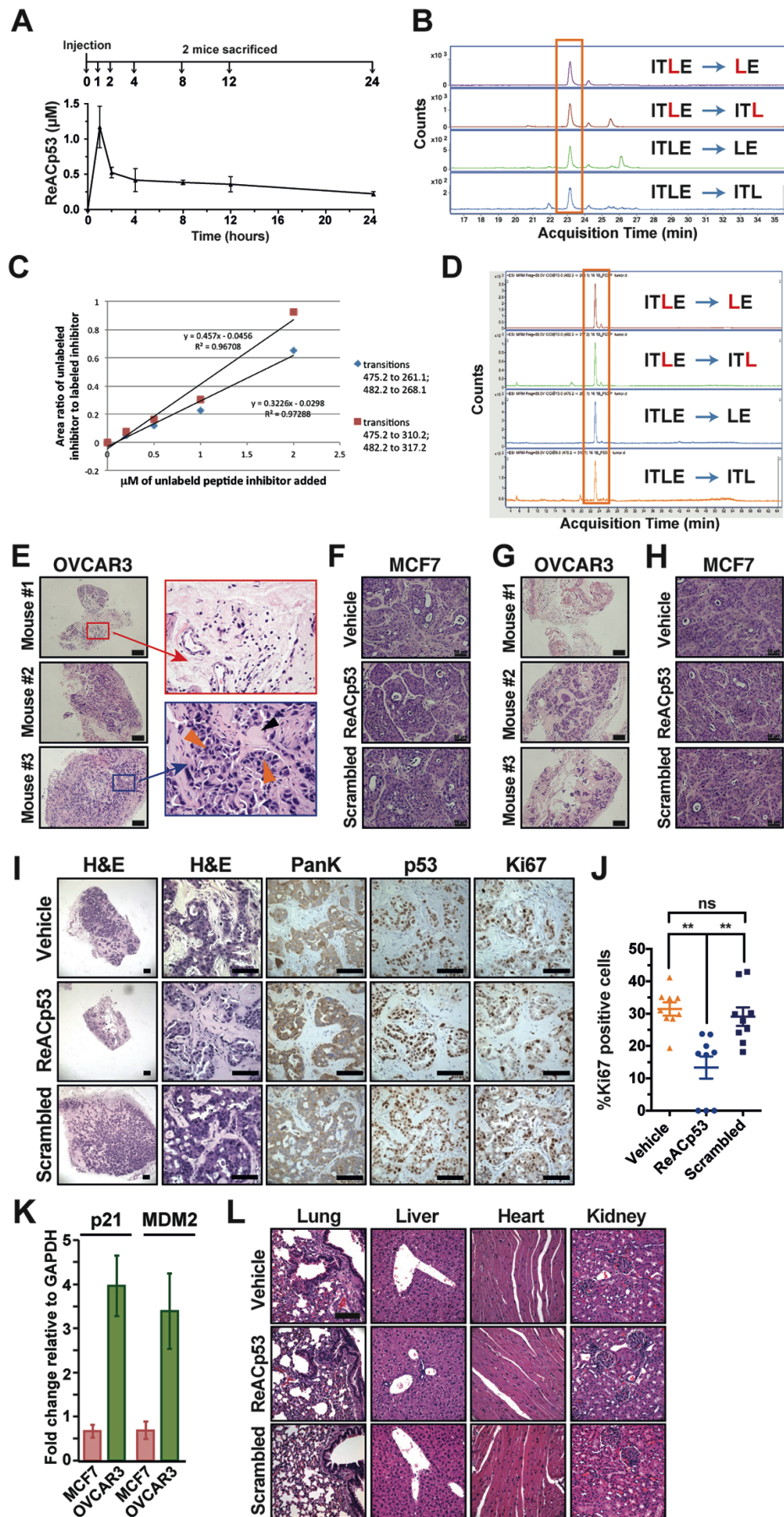


Figure S6 (Refers to Figure 6). Detection of ReACp53 *in vivo* by Multiple Reaction Monitoring (MRM) assay and *in vivo* effects on two xenograft models. **A.** Pharmacokinetics profile of ReACp53 shows relative stability in mouse blood when administered IP. **B.** Serum samples. The top two panels show the MRM traces for the ReACp53 internal standard (IT*LE→LE and IT*LE→IT*L; *L is ¹⁵N/¹³C labeled L, indicated in red), and the bottom two panels show the corresponding MRM traces for ReACp53 which was injected in the mouse one hour prior to sacrifice. **C.** Calibration curve for the MRM experiments. The same two transitions were monitored for each peptide. **D.** Tumor samples. The presence ReACp53 was detected in tumor samples at the one hour time points. The representative figure shows the detection in 5.8 mg of tumor tissue. The presentation is the same as in B. **E.** Histology of pre-established OVCAR3 xenografts (treatment experiment) treated with ReACp53 shows one case with no detectable residual tumor (magnification boxed in red) and two partial responses (magnification in blue). In the partial responses, clear signs of cell death and apoptosis are visible such as pyknotic nuclei (orange arrowheads). In addition, a large proportion of Matrigel is present in the residual xenografts (black arrowhead). Scale bars: 200 μm. **F.** MCF7 xenografts from the treatment experiment show comparable histology across all treatment groups. Scale bars: 50 μm. **G. and H.** Similar results to A. and B. were observed for minimal residual disease model. Scale bars: (C) 200 μm, (D) 50 μm. **I. and J.** Residual xenografts harvested at the end of the minimal residual disease protocol. ReACp53 treated samples had lower Ki67 positive cells than controls as quantified in J. Representation as in Figure 6E. Scale bars: 50 μm. **K.** Quantitative PCR analysis for vehicle and ReACp53 treated residual xenografts derived from the minimal residual disease protocol. p21 and MDM2 were significantly induced upon ReACp53 treatment (green bars) but not vehicle (red bars) only in tumors bearing the R248Q p53 protein (OVCAR3). **L.** H&E. Histological examination of major organs showed no sign of toxicity upon ReACp53 treatment. Scale bar: 100 μm, applies to all panels.

Table S6 (Refers to Figure 6). Blood analysis of mice (n=3) carrying established xenografts treated with vehicle or ReACp53.

Established xenografts																						
		LDH	ALT	AST	ALB	ALP	DBILI	BUN	CREA	GLU	TP											
Vehicle	average	1582.00	483.33	767.10	3.33	68.23	0.60	22.67	0.26	291.33	5.43											
	std	668.19	351.25	513.10	0.29	3.40	0.20	3.51	0.03	48.00	0.38											
ReACp53	average	759.67	167.70	232.53	3.30	85.97	0.27	25.33	0.29	244.33	5.27											
	std	157.60	64.41	94.09	0.10	21.33	0.06	1.53	0.03	24.85	0.21											
		WBC	NE	NE %	LY	LY %	MO	MO %	EO	EO %	BA	BA %	RBC	HB	HCT%	PLT	MCV	MCH	MCHC	RDW%	MPV	PDW
Vehicle	average	1.87	1.60	83.99	0.18	10.70	0.06	3.44	0.02	1.34	0.01	0.52	8.82	12.47	47.90	1112.33	54.30	14.13	26.03	17.93	4.60	19.80
	std	0.80	0.81	5.66	0.02	3.51	0.02	1.27	0.02	1.10	0.01	0.46	0.09	0.12	0.78	133.81	0.36	0.21	0.57	0.31	0.10	0.60
ReACp53	average	4.23	3.33	79.11	0.78	18.04	0.10	2.39	0.02	0.43	0.00	0.03	8.86	12.83	47.20	1397.00	53.27	14.47	27.17	17.57	4.80	19.20
	std	1.07	1.27	21.02	0.93	20.75	0.03	0.39	0.01	0.13	0.00	0.01	0.10	0.06	0.00	121.79	0.67	0.15	0.12	0.15	0.10	0.00

SUPPLEMENTAL EXPERIMENTAL PROCEDURES

Crystallization and structure determination of LTIITLE and TIITLE peptide segments.

Synthesized peptides of greater than 97% purity were dissolved in 10 mM lithium hydroxide, and crystallization screens were carried out at 18°C by hanging-drop vapor diffusion. Peptide 252-LTIITLE-258 was dissolved to a concentration of 2 mg/ml and crystallized in the presence of 0.1 M Tris buffer pH 8.5 and 20% ethanol. Crystals were cryoprotected with 20% glycerol and mounted on 20-50 μ m Mitegen LD loops (Ithaca, NY) before being flash cooled in liquid nitrogen. Crystals of peptide 253-TIITLE-258 formed at a concentration of 6 mg/ml in the presence of 0.01 M zinc chloride, 0.1 M MES buffer pH 6, and 20% PEG 6000. These crystals were mounted on the ends of pulled glass capillaries in the presence of 20% glycerol and left at room temperature. X-ray diffraction data for both peptides was collected at 100 K at beamline 24-ID-E of the Advanced Photon Source (APS) at Argonne National Laboratory using a microfocus beam size of 5x5 μ m². XDS/XSCALE (Kabsch, 1993) and DENZO/SCALEPACK (Otwinowski and Minor, 1997) program packages were used to index, integrate, and scale the reflections. The merged scaled data was imported into CCP4 format (Collaborative Computational Project, 1994) and the program PHASER was used to determine the phases by molecular replacement using a polyalanine beta-strand as the search model (Read, 2001). Structure refinement was performed using REFMAC5 (Murshudov et al., 1997), and PHENIX (Adams et al., 2010); model building and illustrations were performed with COOT (Emsley and Cowtan, 2004) and PYMOL (Delano, 2002), respectively. We thank M. Capel, K. Rajashankar, N. Sukumar, J. Schuermann, I. Kourinov and F. Murphy at NECAT beamlines 24-ID at APS supported by grants from the National Center for Research Resources (5P41RR015301-10) and the NIH National Institute of General Medical Sciences (8 P41 GM103403-10). Use of the APS is supported by DOE under contract DE-AC02-06CH11357. The authors acknowledge the use of the UCLA X-ray Crystallography Core Facility supported by DOE Grant DEFC02-02ER63421 and of instruments at the Electron Imaging Center for NanoMachines supported by NIH (1S10RR23057) and CNSI.

Thioflavin T aggregation assay. The p53 target segment LTIITLE and the p53 aggregation inhibitors including LTRITLE were chemically synthesized, lyophilized and dissolved in 10 mM LiOH at a concentration of 2 mg/ml. All inhibitors tested in this assay were composed of the active sequence only, without the polyarginine tag and RPI linker. Aggregation reactions were performed in these final conditions: 0.7 mg/ml LTIITLE peptide, 7.5 mM LiOH, 100 μ M Tris pH 7.4, 50 μ M Thioflavin T and different concentrations of inhibitors ranging from 1:10 to 10:1 target:inhibitor ratios. All samples were measured in triplicates, and reactions were assembled on ice with pre-chilled buffers and reagents. Due to the fast kinetics of aggregation, the highly hydrophobic segment LTIITLE was added last to each tube just prior measuring. Plates were quickly moved to a SpectraMax M5 (Molecular Devices). Reads were performed every 2 minutes with a 3s shaking time before each read. Parameters were as follows: excitation wavelength 440 nm; emission wavelength 480 nm, temperature 30°C.

Sequencing of p53 in cell lines and patients' biopsies. Genomic DNA was extracted and purified according to manufacturer's instructions (Qiagen). The entire p53-coding region was sequenced using the primers reported in Frebourg et al., 1995.

Peptide preparation for cell experiments and *in vivo* work. ReACp53 was obtained from either GL Biochem or American Peptide. We tested two different counterions, TFA and

acetate, with similar results. For the TFA salt, ReACp53 was dissolved in DMSO at a concentration of 10 mM and filtered using 0.22 μ m Ultrafree-MC spin filter (Millipore). The ReACp53 acetate salt was dissolved in PBS at pH 8.5 at a concentration of 5 mM (final pH ~7.5) and filtered using a 0.22 μ m Steriflip vacuum filter (Millipore). Additional purification steps to remove synthesis contaminants are performed as follows: ReACp53 is diluted to 264 μ M and extensively dialyzed in PBS at pH 7.4 using Slide-A-Lyzer cassettes with 2 kDa cutoff. The peptide is then filtered again using a 0.22 μ m Steriflip vacuum filter (Millipore).

Immunofluorescence. Primary cells were seeded on glass coverslips. Cells untreated or treated for 16-20h with 10 μ M FITC-ReACp53 were fixed in 2% formaldehyde in PBS for 15 minutes. After a 10 min permeabilization step (1% normal goat serum, 1% BSA, 0.1% saponin in PBS), cells were blocked for 30 minutes in the same buffer with 5% normal goat serum. A combination of DO-1 antibody (1:100) and PAb240 (5 μ g/ml) was used to detect the entire pool of p53. Primary antibodies were incubated overnight in 1% normal goat serum, 1% BSA, 0.1% saponin in PBS at 4°C. Secondary antibodies (Jackson ImmunoResearch) were incubated for 45 minutes at room temperature at a 1:250 dilution.

OVCAR and S1 GODL cells were seeded at a 70'000 cells/ml concentration (250 μ l for 17'500 cells/well) in Millicell EZ 8-wells slides (Millipore) and treated with 0, 2, 5 and 10 μ M ReACp53 for 16-20 hours before fixation. Treatment with different concentrations of ReACp53 was performed after changing the media to PrEGM (Lonza). Fixation and staining were performed as reported above. Antibodies used were as follows: DO-1 anti-p53 (1:100, SantaCruz); PAb240 anti-mutant p53 (6 μ g/ml, Millipore); secondary anti-mouse & anti-rabbit (1:250, Jackson ImmunoResearch). Nuclei were counterstained with Hoechst or DAPI. Images were acquired with an Axio Observer D1 microscope (Zeiss). For quantification, 3-5 different fields of view were imaged and total number of cells was counted. For each field of view, we then counted the total number of positive cells (DO-1 or PAb240, depending on the experiment). The number of p53-positive cells was expressed as % of the total number of cells. The values obtained for the 3-5 different fields of view were averaged and the values expressed in % \pm SD.

YO-PRO-1/PI/Hoechst staining. For microscopy, 20'000 cells were seeded in each well of an 8 wells EZ Slide (Millipore) and handled as reported above. The stain was performed on unfixed cells, by adding 3 μ l of the master reaction (2.4 μ l YO-PRO-1, 2.4 μ l PI and 2.4 μ l Hoechst in 65 μ l of water) to each well. The dyes were part of the Chromatin Condensation/Membrane Permeabilization/Dead Cells Apoptosis kit (Life Technologies). For quantification via flow cytometry, cells were plated in 6 well plates at a concentration of 250'000 live cells/well and let adhere for 24h. After overnight treatment, cells were trypsinized, stained according to manufacturer's instructions (Chromatin Condensation/Membrane Permeabilization/Dead Cells Apoptosis kit, Life Technologies) and quantified using a BD LSRII cytometer.

MTS assays. Cells were seeded in 96-well plates at a final concentration of 7'000 live cells/well in 100 μ l of medium supplemented with serum. After 12-16 hours medium was completely removed and after one wash in serum free medium, 100 μ l of PrEGM (Lonza) was added to the wells (serum free). For treatment of samples, ReACp53 dissolved in 100% DMSO and filtered through a 0.22 μ m filter, was added to triplicates or quadruplicate wells to final concentrations of 0, 1, 2, 5 and 10 μ M. Given that the peptide is internalized by all cells present, higher ratio of cells:ReACp53 may result in different EC₅₀, so for ease of comparison, a cell concentration of 70'000 cells/ml was used for all MTS and WB

experiments. Scrambled peptide control or poly-arginine tag control were prepared and used in the same way. Peptides were frozen and thawed twice before being discarded. For Nutlin-3 treatment, Nutlin-3 (Sigma) was dissolved in 100% DMSO and added to triplicate wells at final concentrations of 0, 5, 10, 25 or 50 μ M. After 5 hours of treatment with Nutlin-3 alone, ReACp53 or vehicle was added to the cells. After 16-20 hours incubation at 37°C and 8% CO₂, 20 μ l of pre-warmed MTS solution (CellTiter 96® AQueous One Solution Cell Proliferation Assay, Promega) was added to the wells and incubated for an additional 2 hours at 37°C. After 5s mixing, absorbance at 490 and 650 nm was read with a SpectraMax M5 plate reader (Molecular Devices). Background absorbance at 650 nm was subtracted and values were averaged and normalized to vehicle. t-tests were performed to assess significance.

Uterine fibroblast infection and analysis. The FU-DNp53 CGW lentivirus carrying the R175H p53 gene was a kind gift from Dr. Jiaoti Huang, UCLA. FU-CGW lentivirus production and titration were conducted as previously described. (Memarzadeh S. et al., 2007). Primary human uterine fibroblasts were obtained from ATCC (PCS-460-010), maintained and passaged according to ATCC guidelines and discarded after 3-4 passages. Cells were infected at an MOI of 40 with GFP or DNp53 GFP virus for 16 hours followed by removal of the virus. Cells were harvested and sorted for GFP expression 72h hours after infection using a BD FACS ARIA. Sorted cells were plated in the in vitro 3D organoid assay at a density of 10,000 cells/well in a 24 well plate and treated as described for the tumor organoids. After two days of treatment with peptide, cells were analyzed for AnnexinV and PI staining by flow cytometry on a BD LSRII cytometer. Data was normalized to vehicle treated controls.

Xenograft assays. *Treatment and Minimal Residual disease models:* tumors were established in a subcutaneous xenograft model by injecting 5×10^5 OVCAR3 or MCF7 cells suspended in 100 μ l 1:1 PrEGM:Matrigel in the flank subcuticular space of immunocompromised mice. Tumor bearing mice were treated with daily intraperitoneal injection of vehicle (PBS/0.9% DMSO), 15 mg/kg ReACp53 or scrambled peptide in PBS/0.9% DMSO. Tumor size was measured by calipers. At the end of the therapeutic course, mice were sacrificed. Blood was obtained by cardiac puncture. Xenografts and major organs were portioned and then snap frozen or fixed in 10% buffered formalin. *Cell death assays:* tumors were generated by injecting 1×10^6 S1 GODL cells suspended in 100 μ l of a 1:1 PrEGM:Matrigel suspension in the flank of immunocompromised mice. Each mouse had 3 implants and tumors were allowed to grow for six weeks prior to treatment initiation. In order to detect early apoptotic changes in the tumors, mice were treated for 9 consecutive days with 30 mg/ml ReACp53 (ammonium acetate salt in PBS) or vehicle (PBS). Mice were sacrificed following treatment and xenografts were processed as described above.

TUNEL staining. Sections from S1 GODL xenografts described above were processed using the Roche In Situ cell death detection kit with permeabilization performed by incubating for 8 minutes in 0.1% Triton X-100, 0.1% sodium citrate. Sections were counterstained and mounted using Vectamount with DAPI (Vector Laboratories). Positively stained cells were identified by bright fluorescence co-localized to a DAPI positive nucleus. A total of 5 fields of view sampling all xenografts at 40x were scored for total DAPI positive tumor cells and DAPI/TUNEL double positive cells.

Disseminated disease HGSOc tumor model. Animals were injected intraperitoneally with

2.5×10^6 S1GODL cells suspended in 200 μ l PrEGM (Lonza). Two weeks after cell injection a 3 week treatment course was initiated. In order to eliminate possible confounding toxic effects of DMSO, the ammonium acetate salt of ReACp53 was dissolved in aqueous buffer at a 5mM concentration, and diluted in PBS at pH 7.4 prior injection. Therefore, mice were divided in three groups and treated daily with intraperitoneal injection of vehicle (PBS), 15 mg/kg ReACp53 or scrambled peptide in PBS. For IP sampling experiments, on the 3rd day of treatment, 30 minutes after a vehicle or peptide injection, 1 ml of warm sterile saline was injected intraperitoneally into isoflurane anesthetized mice using a 20G over the needle catheter. Following gentle rocking of the animal, 500 μ l of fluid and cells was withdrawn and analyzed by flow cytometry for Annexin V and PI (BD Biosciences) staining or cell cycle analysis (Muse Cell Cycle Kit, Millipore – see below for more details). At the end of the 3-week time course, the mice were sacrificed. Blood was collected by cardiac puncture. Cells were collected from the peritoneal cavity by peritoneal lavage with up to 5 ml of sterile DMEM/ 10% FBS. 10% of the cells collected were plated in RMPI/10% FBS. After one week, cells were fixed for 10 minutes in 4% PFA. IHC to detect p53 was performed on the plated cells. The remaining 90% of cells from the pelvic lavage were pelleted and fixed for 10 minutes in 10% formalin. Fixed cells were suspended in Histogel, embedded and sectioned. Organs were harvested and fixed for 24 hours in 10% formalin. Implantation on organs was scored for cells staining positive for p53 by examining 5 slides for each mouse taken at 5 different levels within the organs. Detection of any number of cells was scored as a positive implant.

Western Blots. Cells were seeded in 6 wells plates at 250'000 cells/well and 3.6 ml total medium supplemented with serum was added (final cell concentration of 70'000/ml). After 24 h of incubation and one wash in PrEGM medium (Lonza), medium was replaced in 3.6 ml of fresh PrEGM containing 0, 1, 2, 5, 10 μ M ReACp53 or scrambled control peptide. Lysates used for cell cycle phospho-protein evaluation were incubated for 4-5 hours with the peptides. For all other experiments, cells were incubated for 20 hours, trypsinized using 0.05% Trypsin/EDTA (Life Technologies) and spun. Cell lysates were obtained by resuspending the pellets in RIPA buffer (Thermo Fisher) supplemented with HALT protease and phosphatase inhibitors (Thermo Fisher). After vortexing shortly, lysates were incubated for 30 minutes on ice and cleared by centrifugation (30min, 14'000 rpm, 4°C). Protein concentration was determined by Bradford assay (Pierce Microplate BCA Protein Assay Kit – Reducing Agent Compatible, Pierce). Nupage 4-12% SDS-page gels (Life Technologies) were loaded with 4 μ g/well (for p53 stain) or 10 μ g/well (for p73 or THBS1 stain) of lysates and run according to manufacturer's instructions. Proteins were transferred to PVDF membranes using the iBlot2 transfer system (Life Technologies). Western Blots were performed using the iBind system (Life Technologies) and the iBind solution according to manufacturer's instructions. The following antibodies were used: DO-1-HRP-conjugated antibody (anti-p53, Santa Cruz): 7.5 μ l in 2 ml of iBind solution; anti-GAPDH (clone 258, Life Technologies): 1 μ l in 2 ml of iBind solution; anti-p73 (clone p73-9F7, Life Technologies): 30 μ l in 2 ml of iBind solution; anti-thrombospondin (ab85762, Abcam): 10 μ l in 2 ml of iBind solution; anti-phosphoRb (Ser608/611) (clone D20B12, #8516, Cell Signaling): 10 μ l in 2 ml of iBind solution; anti-phosphoChk2 (Thr68) (clone C13C1, #2197, Cell Signaling): 10 μ l in 2 ml of iBind solution. Secondary anti-mouse and anti-rabbit antibodies (Life Technologies) were used at a 2 μ l/ml concentration, 2 ml of iBind solution total. Antibodies were detected with SuperSignal West Pico Chemiluminescent Substrate (Pierce).

Protein Immunoprecipitation. For immunoprecipitation, 75-200 µg of native lysates (Pierce IP Lysis Buffer) were incubated overnight at 4°C with 5 µl of agarose-conjugated PAb240 (sc-99, Santa Cruz Biotechnology) on a rotator. After collecting the immunoprecipitated complexes by centrifugation followed by washes in PBS, samples were resuspended in 20-40 µl of gel loading buffer (Life Technologies). WB with DO-1 was performed as indicated above.

p53 stability/aggregation experiment. 200 µg of native lysates were brought to a 500 µl volume in IP buffer (Pierce) and heated at 42°C in the presence of vehicle or 20 µM ReACp53 for 10 minutes, followed by a 30 minute incubation on ice. p53 was immunoprecipitated overnight using 5 µg of PAb240 (Santa Cruz Biotechnologies) at 4°C on a rotator. Immunoprecipitated complexes were purified with Pierce Direct Magnetic IP/Co-IP Kit according to manufacturer instructions.

Immunohistochemistry. Formalin fixed paraffin embedded tissue sections were treated by heat-induced epitope retrieval in 10 mM citrate buffer pH 6 for antigen recovery, then blocked with 8% normal goat serum on PBS. Slides were incubated overnight at 4°C in primary antibody using the following dilutions: anti-pancytokeratin, 1:750 (Sigma C-1801); anti-p53, 1:200 (Santa Cruz sc-126); anti-Ki67, 1:1000 (Vector Laboratories VP-K451); anti-Bax, 1:250 (Santa Cruz sc7480). Primary antibodies were followed by sequential 45 min incubations at room temperature in biotinylated secondary antibody and streptavidin-horseradish peroxidase. Signal was visualized upon incubation with the DAB substrate. Stained slides were imaged on an Olympus BX51 upright microscope equipped with Optronics Macrofire CCD camera and Optronics PictureFrame software. To determine proliferative index, total and Ki67 positive tumor epithelial cells were scored on 3 high-power fields per graft, and reported as % Ki67 positive cells. Results are reported as average proliferative index for all grafts in each treatment group ± SEM.

Cell Cycle Analysis. 250'000 S1 GODL cells were seeded in 6 wells plate and let adhere for 24 hours. After one wash in serum free medium, 3.6 ml/well of PrEGM±ReACp53 or scrambled peptide at a 5 µM concentration was added. After 4-5 hours, cells were washed in cold PBS and 800 µl of trypsin (Trypsin-EDTA for primary cells) was added to each well. After 5-10 minutes at 37°C, cells were pipetted to yield a single cell suspension and 800 µl of neutralization medium was added to the wells (Trypsin Neutralizing Solution, ATCC). Cells were spun at 150g for 5 minutes, and after one wash in 1ml of cold PBS, fixed in 300 µl of 70% ice-cold ethanol. Samples were kept at -20°C until measured. For cell cycle analysis, cells were stained with 200 µl of Muse Cell Cycle Reagent (Millipore) for 30 minutes at room temperature and measured with a Muse flow cytometer (Millipore). Cells derived from pelvic lavage of mice bearing IP disseminated tumors were spun and processed in a similar fashion.

qPCR. RNA was isolated from xenografts using the Qiagen RNeasy Micro Kit according to manufacturer's instructions. 0.5 µg of RNA was converted to cDNA with the Superscript III First Strand Synthesis kit (Life Technologies). Quantitative-PCR was performed using the iQ SYBR Green Supermix for Real-Time PCR (Bio-Rad) on a Bio-Rad iCycler with iQ5 2.0 Standard Edition Optical System software with the follow primer sets: p21F 5'-ATGTGTCCTGGTTCCCGTTTC-3', p21R 5'-CATTGTGGGAGGAGCTGTGA-3'; Mdm2F 5'-ACCTCACAGATTCCAGCTTCG-3', Mdm2R 5'-TTTCATAGTATAAGTGTCTTTTT-3'; GADD45BF 5'-TACGAGTCGGCCAAGTTGATG-3', GADD45BR 5'-GGATGAGCGTGAAGTGGATTT-3'; PUMAF 5'-GACCTCAACGCACAGTACGAG-3', PUMAR

5'-AGGAGTCCCATGATGAGATTGT-3'; GAPDHF 5'-AGCCACATCGCTCAGACAC-3', GAPDHR 5'-GAGGCATTGCTGATGATCTTG-3'. Data were analyzed by using the $\Delta\Delta C_T$ method with normalization to the housekeeping gene GAPDH.

Peptide Synthesis for MRM analysis. Unlabeled peptides were purchased by GL Biochem. Labeled forms of RRRRRRRRRRPILTRIT{*L}E (ReACp53) and the corresponding scrambled peptide RRRRRRRRRRRITTRPI{*L}E were synthesized in-house using Fmoc chemistry. The residue designated {*L} is Fmoc-L-leucine-OH- $^{13}\text{C}_6$, ^{15}N (cat #593532, Sigma-Aldrich) and was used for preparation of the labeled forms. Peptides were purified by reverse phase HPLC. Molecular weights of the purified peptides were confirmed by MALDI-TOF. Unlabeled peptides were purchased by GL Biochem. Labeled forms of RRRRRRRRRRPILTRIT{*L}E (ReACp53) and the corresponding scrambled peptide RRRRRRRRRRRITTRPI{*L}E were synthesized in-house using Fmoc chemistry. Unlabeled forms of ITLE and PILLE were prepared by trypsin digestion of ReACp53 (42.4 nmol) and scrambled peptide (366 nmol), respectively, in ammonium bicarbonate (50 mM, 500 μL) with TPCK-treated trypsin (Sigma-Aldrich: 1 nmol and 9 nmol for ReACp53 and scrambled peptide, respectively, 37°C, overnight). The digestion mixtures were subjected to reverse phase chromatography and the collected fractions were screened by ESI/MS. Fractions containing the signals of interest were m/z 475 for ITLE from ReACp53 (m/z 599 for PILTR from ReACp53 not found), and m/z 490 for ITTR and m/z 584 for PILLE from the scrambled peptide were collected. The MS/MS spectra of ITLE and PILLE from ReACp53 and scrambled peptide, respectively, were recorded, and the LC/MS/MS-MRM assay was optimized using these purified peptides.

Sample preparation for MRM analysis. Mice (n=14) were injected with 15 mg/kg ReACp53 intraperitoneally and sacrificed at 1, 2, 4, 8, 12 and 24h post-injection. Blood was collected by cardiac puncture and serum was recovered by incubating samples on ice followed by centrifugation. Tumor samples were grinded with BioMasherII micro grinders (Kimble Chase) prior to mild sonication. Samples were spun, and the supernatant was treated identically to the serum samples according to the following protocol. Serum/tissue samples (50 μL , in duplicate, each sample from a separate mouse) were spiked with 50 pmoles of each {*L}-labeled peptide (internal standards) in an eppendorf tube. In order to solubilize ReACp53 and precipitate all other proteins the following procedure was performed. Ammonium acetate (6 μL , final conc. 0.5 M) was added and the samples were incubated in a water bath sonicator for 30min. Methanol (150 μL) was added and the mixture vigorously mixed and incubated for 30 minutes in a water bath sonicator, followed by centrifugation (20,000g, 10 min). The supernatant was transferred to a clean tube and the sample was dried in a vacuum centrifuge. The pellet was re-suspended in sodium bicarbonate (50 μL , 50 mM, pH 8.0) and digested with TPCK-treated trypsin (1 nM, 37°C, overnight). The digest was dried in a vacuum centrifuge and the residue was resuspended in solvent A (99:1 water:acetonitrile with 0.1% formic acid, v/v, 50 μL). After vigorous mixing (2 min), the samples were centrifuged (20,000g, 5 min) and the supernatants were transferred to HPLC injector vials. With each batch of serum or tissue samples a series of standards were prepared in which unlabeled-ReACp53 and – scrambled peptide (0, 10, 25, 50, and 100 pmol, in duplicates) were added to naive plasma (50 μL), along with the same amount of the labeled peptide internal standards (50 pmoles of each). These samples were processed as described above.

Combined liquid chromatography-tandem mass spectrometry with multiple reaction monitoring (MRM). Aliquots of the digested samples (5 μL) were injected onto a reverse

phase HPLC column (Phenomenex Kinetex C18, 1.7m, 100x2.1mm) equilibrated in solvent A and eluted (100 μ L/min) with a linearly increasing concentration of solvent B (acetonitrile/formic acid, 100/0.1, v/v: min/%B; 0/0.1, 10/0.1, 50/50, 53/99, 56/0.1, 66/0.1). The effluent from the column was directed to an electrospray ion source (Agilent Jet Stream) connected to a triple quadrupole mass spectrometer (Agilent 6460) operating in the positive ion tandem mass spectrometric multiple reaction monitoring (MRM) mode in which the intensity of preselected parent fragment transitions were recorded with instrument manufacturer-supplied software (Mass Hunter).

Two transitions were chosen for each peptide; m/z 475.2 \rightarrow 310.1 (ITLE \rightarrow ITL) and 475.2 \rightarrow 261.1 (ITLE \rightarrow LE) for ReACp53, m/z 584.2 \rightarrow 437.2 (PILLE \rightarrow PILL) and 584.2 \rightarrow 324.2 (PILLE \rightarrow PIL) for scrambled peptide, m/z 482.2 \rightarrow 317.1 (IT{*L}E \rightarrow IT{*L}) and 482.2 \rightarrow 268.1 (IT{*L}E \rightarrow {*L}E) for labeled- ReACp53, and m/z 591.2 \rightarrow 444.2 (PIL{*L}E \rightarrow PIL{*L}) and 591.2 \rightarrow 331.2 (PI{*L}E \rightarrow PI{*L}) for labeled-scrambled peptide. As described above, each MRM transition had been previously optimized with the unlabeled peptides for maximal response (collision energy, fragmentor voltage and collision cell accelerator voltage). Under these chromatographic conditions the tryptic fragments from ReACp53 (ITLE) and scrambled peptide (PILLE) eluted at 28.4 and 30.4 min, respectively.

The areas of each peak were integrated and recorded. A standard curve constructed from the data obtained from the standards in which the ratio of peptide peak area/internal standard peak area was plotted against the amount of peptide in each standard. The amount of each peptide in the samples was then derived by interpolation from the standard curve. Signal intensity for the scrambled peptide was significantly less than for ReACp53. It was possible to measure the concentration of the scrambled peptide at the 1 hour time point to be 1.20 \pm 0.1 μ M. The other time points had peaks for the transitions, but they were too low in intensity to accurately measure.

Sample preparation for RNAseq. OVCAR3 and MCF7 cells were trypsinized, spun and resuspended in a 1:1.33 mixture of PrEGM media (Lonza CC-3166) and Matrigel (BD Biosciences). OVCAR3 cells carry the R248Q p53 mutation, that retains the potential to function similarly to the WT-counterpart and induce transcription of p53 target genes upon pharmacological treatment with p53-targeting molecules (Zhao et al, 2010; Jones et al, 2012; Mohell et al, 2015). High-grade serous cancers, obtained from consented patients, were dissociated to single cells by enzymatic digestion and resuspended at the same concentration as above. 70 μ L of the PrEGM:Matrigel mixture, containing a total of 100'000 cells, was plated in triplicates around the rim of a 24-well cell culture dish and overlaid with 1ml PrEGM. After a 2 days incubation at 37°C and 8% CO₂, medium was removed and exchanged with a 1ml of fresh PrEGM containing either vehicle (DMSO) or 5 μ M ReACp53. After 24 hours, a second treatment was performed by completely removing the medium and replenishing with fresh PrEGM containing vehicle or ReACp53. After two treatments (48h total), cells were released by dispase treatment (Life Technologies) and resuspended in RNALater (Life Technologies). RNA was extracted using the Qiagen RNeasy microkit according to manufacturer's instruction and purity was assessed by absorbance measurements. Total RNA was quantified with the Qubit RNA HS assay kit (Life Technologies) and converted to cDNA using SuperScript III (Life Technologies) after a DNase treatment. mRNA libraries were prepared for each triplicate with the TruSeq RNA v2 kit following Illumina instructions. Sequencing was performed at the UCLA BSCRC High Throughput Sequencing Facility.

Gene Differential Expression Analysis. Tophat (Version 2.0.6; Trapnell et al., 2009) and

Bowtie (Version 0.12.8) were used to align reads to human genome GRCh37/hg19 with Ensembl 75 gene annotation. Reads that were uniquely mapped were counted and quantified by HTSeq-count (Version 0.5.3p9; Anders et al., 2014) with Ensembl 75 gene sets. Gene differential expression analysis was performed using DESeq2 (Version 1.4.5; Love et al., 2014). DESeq applies a negative binomial model which allows to correctly account for biological variability. Genes which had no reads across all samples were discarded. Genes with and with more than 1.5 fold change in expression and an adjusted p-value of less than 0.01 were classified as significantly differentially expressed and analyzed further.

For data representation, the heat maps shown in Figure 5 and Figure S5F representing mRNA expression profiles were generated using the R-package “GENE.E” (<http://www.broadinstitute.org/cancer/software/GENE-E/index.html>) with DESeq2 rlog() function transformed values. The heat map in Figure S5E shows p-values (ReACp53 vs. vehicle) from the four samples and was generated with the R-package “GENE.E” (<http://www.broadinstitute.org/cancer/software/GENE-E/index.html>).

Statistical methods. Means were either evaluated with t tests when comparing two independent groups or using a repeated measure (mixed effects) analysis of variance (ANOVA) model for comparisons over time and group after examination of normal quantile plots to verify that the data followed the normal distribution. The Tukey HSD significance criterion or Holm-Sidak method were used to correct for multiple comparisons under the ANOVA model (see figure text for specific cases). EC₅₀ values and their standard errors were estimated on the log scale using non parametric spline methods (package drc – R library URL: <http://www.r-project.org>, <http://www.bioassay.dk>). The original scale EC₅₀ values and their coefficient of variation (CV) are reported. The EC₅₀ standard errors reflect both within and between experiment variability. The EC₅₀ values were compared across serum levels using a repeated measure (paired) model. Graphs were generated with Prism 6.0 (GraphPad).

SUPPLEMENTAL REFERENCES

Adams, P.D., Afonine, P.V., Bunkóczi, G., Chen, V.B., Davis, I.W., Echols, N., Headd, J.J., Hung, L.-W., Kapral, G.J., Grosse-Kunstleve, R.W., et al. (2010). *PHENIX*: a comprehensive Python-based system for macromolecular structure solution. *Acta Crystallographica Section D Biological Crystallography* 66, 213–221.

Anders, S., Pyl, P.T., and Huber, W. (2014). HTSeq – A Python framework to work with high-throughput sequencing data. *bioRxiv* 002824.

Collaborative Computational Project, Number 4 (1994). The CCP4 suite: programs for protein crystallography. *Acta Crystallogr. D Biol. Crystallogr.* 50, 760–763.

Delano, W. (2002). The PyMOL Molecular Graphics System: <http://www.pymol.org>

Emsley, P., and Cowtan, K. (2004). Coot: model-building tools for molecular graphics. *Acta Crystallogr. D Biol. Crystallogr.* 60, 2126–2132.

Frebourg, T., Barbier, N., Yan, Y.X., Garber, J.E., Dreyfus, M., Fraumeni, J., Li, F.P., and Friend, S.H. (1995). Germ-line p53 mutations in 15 families with Li-Fraumeni syndrome. *Am J Hum Genet* 56, 608–615.

Kabsch, W. (1993). Automatic processing of rotation diffraction data from crystals of initially unknown symmetry and cell constants. *Journal of Applied Crystallography* 26, 795–800.

Jones, R.J., Bjorklund, C.C., Baladandayuthapani, V., Kuhn, D.J., and Orlowski, R.Z. (2012). Drug Resistance to Inhibitors of the Human Double Minute-2 E3 Ligase Is Mediated by Point Mutations of p53, but Can Be Overcome with the p53 Targeting Agent RITA. *Mol Cancer Ther* 11, 2243–2253.

Love, M.I., Huber, W., and Anders, S. (2014). Moderated estimation of fold change and dispersion for RNA-Seq data with DESeq2. *bioRxiv* 002832.

Memarzadeh, S., Xin, L., Mulholland, D.J., Mansukhani, A., Wu, H., Teitell, M.A., and Witte, O.N. (2007). Enhanced paracrine FGF10 expression promotes formation of multifocal prostate adenocarcinoma and an increase in epithelial androgen receptor. *Cancer Cell* 12, 572–585.

Mohell, N., Alfredsson, J., Fransson, Å., Uustalu, M., Byström, S., Gullbo, J., Hallberg, A., Bykov, V.J.N., Björklund, U., and Wiman, K.G. (2015). APR-246 overcomes resistance to cisplatin and doxorubicin in ovarian cancer cells. *Cell Death Dis* 6, e1794.

Murshudov, G.N., Vagin, A.A., and Dodson, E.J. (1997). Refinement of Macromolecular Structures by the Maximum-Likelihood Method. *Acta Crystallographica Section D Biological Crystallography* 53, 240–255.

Otwinowski, Z., and Minor, W. (1997). Processing of X-ray diffraction data collected in oscillation mode. (Elsevier), pp. 307–326.

Read, R.J. (2001). Pushing the boundaries of molecular replacement with maximum likelihood. *Acta Crystallogr. D Biol. Crystallogr.* 57, 1373–1382.

Trapnell, C., Pachter, L., and Salzberg, S.L. (2009). TopHat: discovering splice junctions with RNA-Seq. *Bioinformatics* 25, 1105–1111.

Zhao, C.Y., Grinkevich, V., Nikulenkov, F., Bao, W., and Selivanova, G. (2010). Rescue of the apoptotic-inducing function of mutant p53 by small molecule RITA. *Cell Cycle* 9, 1847-1855.